Article

Chemico-genetic discovery of astrocytic control of inhibition in vivo

https://doi.org/10.1038/s41586-020-2926-0

Received: 23 January 2020

Accepted: 19 August 2020

Published online: 11 November 2020

Check for updates

Tetsuya Takano[1]✉, John T. Wallace[1], Katherine T. Baldwin[1], Alicia M. Purkey[1], Akiyoshi Uezu[1], Jamie L. Courtland[2], Erik J. Soderblom[1,3], Tomomi Shimogori[4], Patricia F. Maness[5,6], Cagla Eroglu[1,2]✉ & Scott H. Soderling[1,2]✉

Perisynaptic astrocytic processes are an integral part of central nervous system synapses[1,2]; however, the molecular mechanisms that govern astrocyte–synapse adhesions and how astrocyte contacts control synapse formation and function are largely unknown. Here we use an in vivo chemico-genetic approach that applies a cell-surface fragment complementation strategy, Split-TurboID, and identify a proteome that is enriched at astrocyte–neuron junctions in vivo, which includes neuronal cell adhesion molecule (NRCAM). We find that NRCAM is expressed in cortical astrocytes, localizes to perisynaptic contacts and is required to restrict neuropil infiltration by astrocytic processes. Furthermore, we show that astrocytic NRCAM interacts transcellularly with neuronal NRCAM coupled to gephyrin at inhibitory postsynapses. Depletion of astrocytic NRCAM reduces numbers of inhibitory synapses without altering glutamatergic synaptic density. Moreover, loss of astrocytic NRCAM markedly decreases inhibitory synaptic function, with minor effects on excitation. Thus, our results present a proteomic framework for how astrocytes interface with neurons and reveal how astrocytes control GABAergic synapse formation and function.

The majority of central nervous system (CNS) synapses are ensheathed by tiny astrocytic processes[1,2]. These astrocytic contacts are an integral functional compartment of the tripartite synapse, which is defined as the combination of pre- and postsynaptic neuronal, and perisynaptic astrocytic, processes[3]. At the synapse, astrocytes control basal synaptic transmission, neuromodulation, ionic balance and neurotransmitter clearance[4–8]. Furthermore, astrocyte and synapse development are interdependent processes that are regulated by dynamic bidirectional intercellular communication via secreted factors and cell adhesion molecules[9–12]. Historically, however, gaining molecular insights into perisynaptic astrocyte–neuron signalling has been hampered owing to the lack of biochemical methods for isolating this astrocytic compartment.

To identify proteins at the extracellular clefts between astrocytes and neurons, we developed a chemico-genetic in vivo BioID (iBioID) approach, based on reconstituting the enzymatic activity of a proximity-biotinylating enzyme, TurboID[13], at astrocyte–neuron junctions (Fig. 1a). Recent studies have shown that split biotinylation constructs could recover enzymatic activity when they were in close proximity in the cell cytoplasm[14,15]. In this study, we used our glycosylphosphatidylinositol-anchored reconstitution-activated proteins highlight intercellular connections (GRAPHIC) strategy[16] to direct N- and C-terminal TurboID fragments to the extracellular surface of neurons and astrocytes (Fig. 1a, Extended Data Fig. 1a). Among the two Split-TurboID construct pairs that we tested in HEK 293T cells (Extended Data Fig. 1a), the biotinylation activity of Split 1-TurboID was higher than that of Split 2-TurboID (Extended Data Fig. 1b, lane 8). We therefore used Split 1-TurboID for the remainder of this study, and named the two molecules N-TurboID and C-TurboID. We also used a GRAPHIC-tagged full-length TurboID construct, TurboID-surface, to biotinylate astrocyte surface proteins (Extended Data Fig. 1a, bottom).

In astrocyte–neuron co-cultures, astrocytes expressing TurboID-surface under the control of the GfaABC1D promoter[17] (Extended Data Fig. 1c) exhibited biotinylation activity along their membranes (Extended Data Fig. 1d). Moreover, the reconstituted activity of Split-TurboID was found only at contact sites between neurons and astrocytes (Extended Data Fig. 1c), but not when either of the halves were expressed alone (Extended Data Fig. 1d). To investigate whether TurboID-surface or Split-TurboID biotinylates tripartite synapses in these cultures, astrocytes were co-transduced with GfaABC1D-mCherry-CAAX to mark astrocyte membranes, and synapses were labelled by immunostaining with pre- and postsynaptic makers (excitatory, VGLUT1 and HOMER 1; inhibitory, VGAT and gephyrin). Both constructs mediated biotinylation that overlapped with astrocytic membranes and closely associated with excitatory and inhibitory synaptic markers (Extended Data Fig. 2a–d), demonstrating the functional reconstitution of TurboID transcellularly at perisynaptic astrocyte–neuron junctions in vitro.

To test their activity in vivo, the constructs were introduced into mouse brain astrocytes and/or neurons via retro-orbital injections

[1]The Department of Cell Biology, Duke University Medical School, Durham, NC, USA. [2]Department of Neurobiology, Duke University Medical School, Durham, NC, USA. [3]Duke Proteomics and Metabolomics Shared Resource and Duke Center for Genomic and Computational Biology, Duke University Medical School, Durham, NC, USA. [4]Molecular Mechanisms of Brain Development, Center for Brain Science (CBS), RIKEN, Saitama, Japan. [5]Department of Biochemistry, University of North Carolina School of Medicine, Chapel Hill, NC, USA. [6]Department of Biophysics, University of North Carolina School of Medicine, Chapel Hill, NC, USA. ✉e-mail: tetsuya.takano@keio.jp; cagla.eroglu@duke.edu; scott.soderling@duke.edu

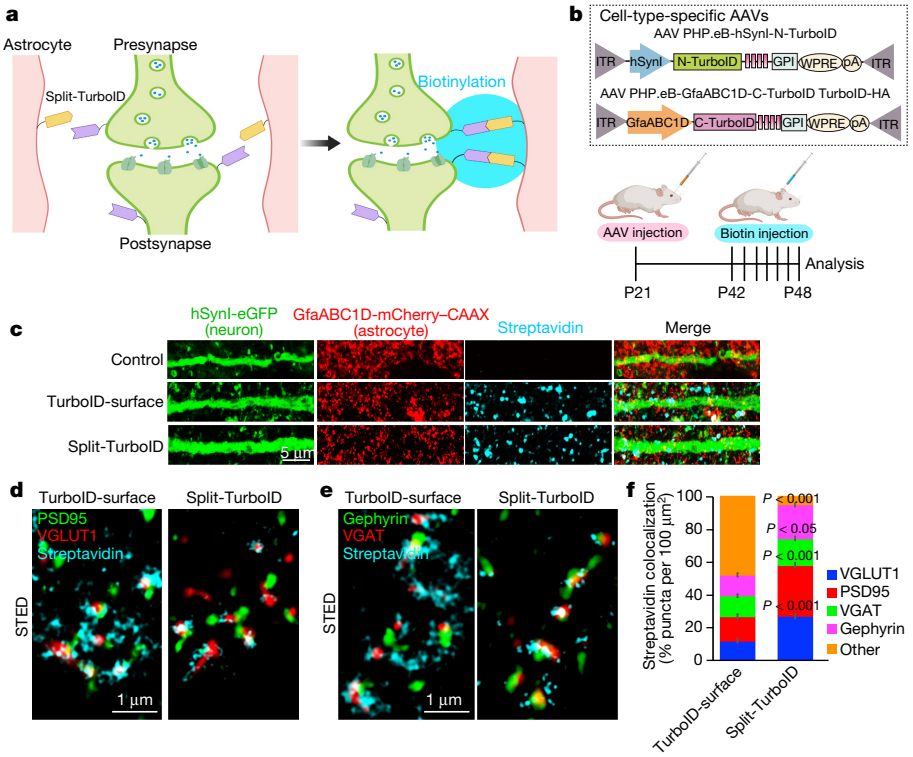

Fig. 1 | Identification of the astrocyte–neuron synaptic cleft proteome using in vivo Split-TurboID. a, Schematic of the Split-surface iBioID approach. **b**, Outline of Split-TurboID method using cell-type-specific AAVs. ITR, inverted terminal repeats; hSyn1, human synapsin 1 promoter; GPI, glycosylphosphatidylinositol; WPRE, woodchuck hepatitis virus post-transcriptional regulatory element; pA, polyadenylation. **c**, Confocal images of cortical expression of Split-TurboID or TurboID-surface coexpressed with neuronal eGFP and astrocyte mCherry–CAAX. **d**, **e**, Three-colour STED images showing biotinylated proteins adjacent to excitatory synaptic markers PSD95 and VGLUT1 (**d**), and inhibitory synaptic markers gephyrin and VGAT (**e**). **f**, The ratio of biotinylated proteins that colocalized with VGLUT1, PSD95, VGAT or gephyrin. $n = 15$ cells per each condition from 3 mice. $n = 3$ biological repeats. Student's paired t-test, comparing TurboID-surface and Split-TurboID. Data are mean ± s.e.m.

of adeno-associated viruses (AAVs)[18] at postnatal day (P)21 (Fig. 1b, Extended Data Fig. 3a–c) and the mice were given subcutaneous biotin injections starting at P42 for 7 days (Fig. 1b)[19]. Biotinylated proteins were detected by immunoblotting and immunohistochemistry (Extended Data Fig. 4a–d) both for astrocyte-specific TurboID-surface and reconstituted Split-TurboID constructs. However, when Split-TurboID fragments were expressed alone, no biotinylation was observed (Extended Data Fig. 4a–c). These results show that the TurboID-surface and Split-TurboID constructs generate extracellular biotinylation in vivo.

To confirm that biotinylated proteins localize to neuron–astrocyte contacts, we labelled neurons with eGFP (using AAV PHP.eB-hSynI-eGFP) and astrocyte membranes with mCherry–CAAX (using AAV PHP.eB-GfaBC1D-mCherry-CAAX) and co-injected either astrocyte-specific TurboID-surface or Split-TurboID-expressing viruses. In both conditions, biotinylated proteins were located at the contacts between astrocytic and neuronal processes (Fig. 1c). Using super-resolution stimulated emission depletion (STED) microscopy, we found that biotinylated proteins surround excitatory and inhibitory synapses (Fig. 1d, e). More than 50% of TurboID-surface-induced biotinylation and more than 90% of Split-TurboID-induced biotinylation was closely associated with synaptic markers (Fig. 1f). The densities of synapses were not affected by either labelling approach (Extended Data Fig. 4e, f). Together, these results show that the TurboID-surface and Split-TurboID constructs effectively biotin-label perisynaptic contacts between astrocytes and neurons in vivo.

Perisynaptic cleft proteome discovery

To identify the tripartite synaptic proteins, proteins biotinylated by Split-TurboID or astrocyte-specific TurboID-surface constructs were purified and analysed by quantitative high-resolution liquid chromatography–tandem mass spectrometry (LC–MS) (Fig. 2a). When combined, the Split-TurboID and astrocyte-specific TurboID-surface datasets identified 776,376 peptides corresponding to 3,171 distinct proteins (Extended Data Fig. 4g). After three independent experiments and following removal of known contaminants[19], 173 and 178 proteins were found to be significantly enriched (1.5. fold) in Split-TurboID and astrocyte-specific TurboID-surface fractions, respectively, compared with soluble TurboID control (Extended Data Fig. 4g–i, Supplementary Tables 1, 2). This enrichment approach is stringent, and thus may not identify all astrocytic proteins that are present at perisynaptic processes, as it selects only those that are overrepresented at synapses compared with other compartments.

A total of 118 proteins were common between the two datasets, yielding a high-confidence tri-partite synapse proteome (Fig. 2b, Extended Data Fig. 4g–i, Supplementary Table 3). This list includes known tripartite synapse proteins such as neuroligin-3 and neurexin-1[9], calcium channel auxiliary subunits that also regulate glutamate receptor trafficking (CACNA2D3, CACNG2 and CACNG3), excitatory synaptic proteins such as AMPA receptors (GRIA2 and GRIA3), and inhibitory synaptic proteins such as type A γ-aminobutyric acid ($GABA_A$) receptors (GABRA1, GABRA4, GABRB2 and GABRG2) (Fig. 2b). By cross-referencing our proteomics data set with cell-type-specific gene-expression databases[20,21], we found that messenger RNA for 33 of these proteins were enriched in astrocytes (RNA-sequencing expression ratio >1.0, diamonds in Fig. 2b), 76 were enriched in neurons (circles in Fig. 2b) and 5 proteins had equal or unknown distribution (Fig. 2b). Bioinformatics analysis showed that our high-confidence tripartite proteome contained known synaptic cleft proteins (29 proteins, 25%), cell adhesion proteins (18 proteins, 15%), channels (18 proteins, 15%), G-protein-coupled receptors and

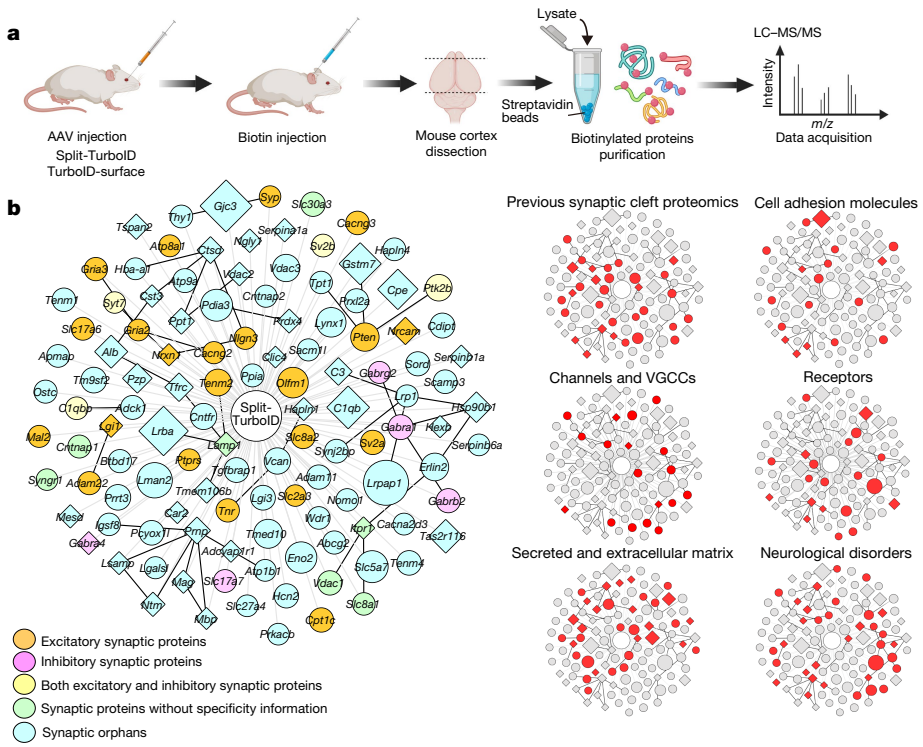

Fig. 2 | The astrocyte–neuron synaptic cleft proteome. a, Outline of proteomic approach. **b**, Left, overlapping high-confidence proteins shared between the Split-TurboID and TurboID-surface enriched fractions. Right, clustergram topology of proteins in selected functional categories. Node titles show the corresponding gene symbols and node size represents $\log_2$ fold enrichment over negative control. Proteins for which gene expression is enriched in neurons (mRNA expression in astrocyte/neuron <1) are in circles, those for which gene expression is enriched in astrocytes (mRNA expression in astrocyte/neuron ≥1.0) are in diamonds. Edges are shaded according to the type of interaction (grey, iBioID; black, previously reported protein–protein interactions).

associated proteins (4 proteins, 3%), other receptors and associated proteins (16 proteins, 14%), secreted or extracellular matrix components (34 proteins, 29%), and proteins encoded by genes implicated in disorders, including autism spectrum disorder and schizophrenia (34 proteins, 29%) (Fig. 2b).

Adhesions between astrocytes and neurons have critical roles in orchestrating the concurrent development of synapses and morphogenesis of astrocytes[9,22]. To identify regulators of this process, we selected teneurin-2 (TENM2), teneurin-4 (TENM4) and NRCAM as candidate bridging molecules between astrocytes and neurons. To deplete target proteins in astrocytes, we used a CRISPR-based approach. We confirmed depletion of astrocytic NRCAM using this approach by quantitative western blot analysis (Extended Data Fig. 5a). NRCAM single guide RNA (sgRNA) in combination with astrocyte-specific Cas9 significantly diminished the level of NRCAM protein in mixed neuron–astrocyte cultures; this could be rescued by re-expression of sgRNA-resistant human NRCAM in astrocytes (Extended Data Fig. 5b, c). Next, we used this astrocyte-specific CRISPR-based approach in vivo to rapidly gain preliminary data on candidate proteins[23] (Extended Data Fig. 5d, e). We retro-orbitally injected AAVs containing sgRNA for each candidate gene together with Cre recombinase under the control of an astrocyte-specific promoter (AAV PHP.eB-U6-sgRNA-GfaABC1D-Cre) into conditional Cas9 knock-in (KI) mice. Astrocyte-specific Cre expression was confirmed in vivo using a tdTomato Cre-reporter line (Extended Data Fig. 5f, g). We used either a negative control virus (AAV-empty sgRNA-GfaABC1D-Cre) or sgRNA virus against each target gene along with astrocyte-specific mCherry–CAAX to quantify astrocyte morphology.

Compared with controls, loss of TENM4 but not TENM2 in P42 mouse cortical astrocytes significantly decreased astrocyte territory volume and the infiltration of fine astrocyte processes into the neuropil (measured by neuropil infiltration volume (NIV)) (Extended Data Fig. 5h–k). By contrast, the deletion of NRCAM significantly increased NIV (Extended Data Fig. 5j, k), indicating that NRCAM is a negative regulator of astrocytic elaboration into the neuropil. Thus, we focused on NRCAM for further analysis.

NRCAM regulates astrocyte morphogenesis

To confirm that endogenous NRCAM is labelled by Split-TurboID in vivo, we used STED imaging, which showed that NRCAM colocalizes with biotinylated proteins in vivo (Extended Data Fig. 6a). NRCAM has previously been identified at contacts between axons and myelinating glia[24,25] and has been studied as a neuronal protein regulating dendritic spine pruning[26,27] but not, to our knowledge, in astrocytes. Cell-type-specific transcriptome analysis shows that levels of mRNA encoding NRCAM are higher in astrocytes than in neurons or oligodendrocytes[20,21]. We confirmed NRCAM protein expression in cultured astrocytes by western blot (Extended Data Fig. 6b). Next, we analysed NRCAM localization in astrocytes in vivo by STED microscopy, observing that endogenous NRCAM puncta colocalized with astrocytic membranes (Extended Data Fig. 6c, d).

NRCAM is known to function in part through a homophilic transcellular interaction[28]. In agreement, when we injected neuron-specific and astrocyte-specific *Nrcam*-expressing viruses into P21 mice (Extended Data Fig. 6e), we observed colocalization of sparsely expressed astrocytic haemagglutinin-tagged NRCAM (NRCAM–HA) with neuronal NRCAM–V5 (Extended Data Fig. 6f) by STED imaging at P42.

NRCAM is also expressed during early postnatal development[26,27]. Deletion of NRCAM from astrocytes during the first two weeks of development significantly increased astrocytic territory size and enhanced NIV when compared with controls (Extended Data Fig. 7a–g). These

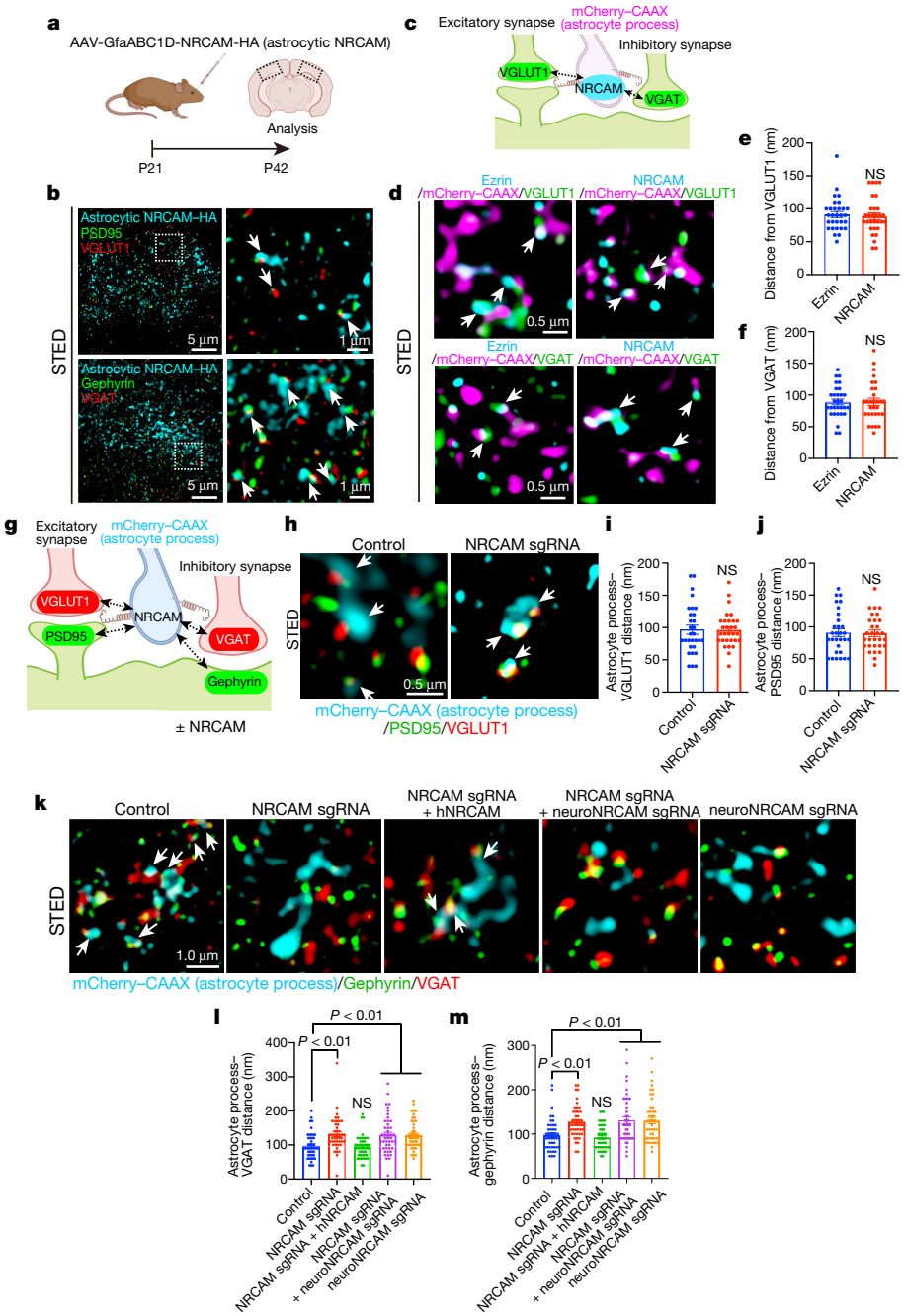

Fig. 3 | NRCAM controls astrocyte-neuron contacts in vivo. a, Schematic of the visualization of astrocytic NRCAM in vivo. **b**, Three-colour STED images demonstrating that astrocytic NRCAM are adjacent to excitatory synapses or inhibitory synapses. **c**, Schematic of astrocytic NRCAM distribution assay in vivo. **d**, Three-colour STED images showing mCherry–CAAX-positive NRCAM or ezrin adjacent to excitatory presynapses and inhibitory presynapses. **e**, **f**, Quantification of average distance between astrocytic NRCAM and VGLUT1 or VGAT ($n = 30$ puncta per each condition from 3 brains). **g**, Schematic of in vivo astrocytic process–neuronal synapses contact assay. **h**–**m**, Three-colour STED images of an astrocytic process following deletion of astrocyte NRCAM adjacent to excitatory synapses (**h**) or inhibitory synapses (**k**). hNRCAM, human NRCAM; neuroNRCAM sgRNA, deletion of neuronal NRCAM. **i**, **j**, **l**, **m**, Quantification of average distance between astrocytic process and excitatory synapses (**i**, **j**) or inhibitory synapses (**l**, **m**) ($n = 30$ puncta per condition from 3 brains). $n = 3$ biological repeats. In **e**, **f**, **i**, **j**, Student's paired t-test. In **l**, **m**, one-way analysis of variance (ANOVA) with Dunnett's multiple comparison. Data are mean ± s.e.m. NS, not significant. Arrows in **b**, **d**, **h**, highlight examples of adjacent synaptic fluorescent signals in the images.

phenotypes were rescued by coexpression of sgRNA-resistant NRCAM–HA in astrocytes (Extended Data Fig. 7b–g). NRCAM is a type I membrane protein with a modular extracellular domain architecture that is composed of repeated immunoglobulin and fibronectin domains (Extended Data Fig. 7b). To determine whether extracellular interactions of NRCAM are required for astrocytic morphogenesis in vivo, we created two deletion mutants of human NRCAM: NRCAM(ΔIG), comprising residues 620–1193 and lacking the immunoglobulin domain; and NRCAM(ΔECD), comprising residues 1030–1193 and lacking both immunoglobulin and fibronectin domains (Extended Data Fig. 7b, c). Neither mutant rescued the morphology of NRCAM-deleted astrocytes (Extended Data Fig. 7d–g), indicating that the extracellular interactions via immunoglobulin domains of NRCAM are necessary for maintaining the wild-type morphology. To test whether

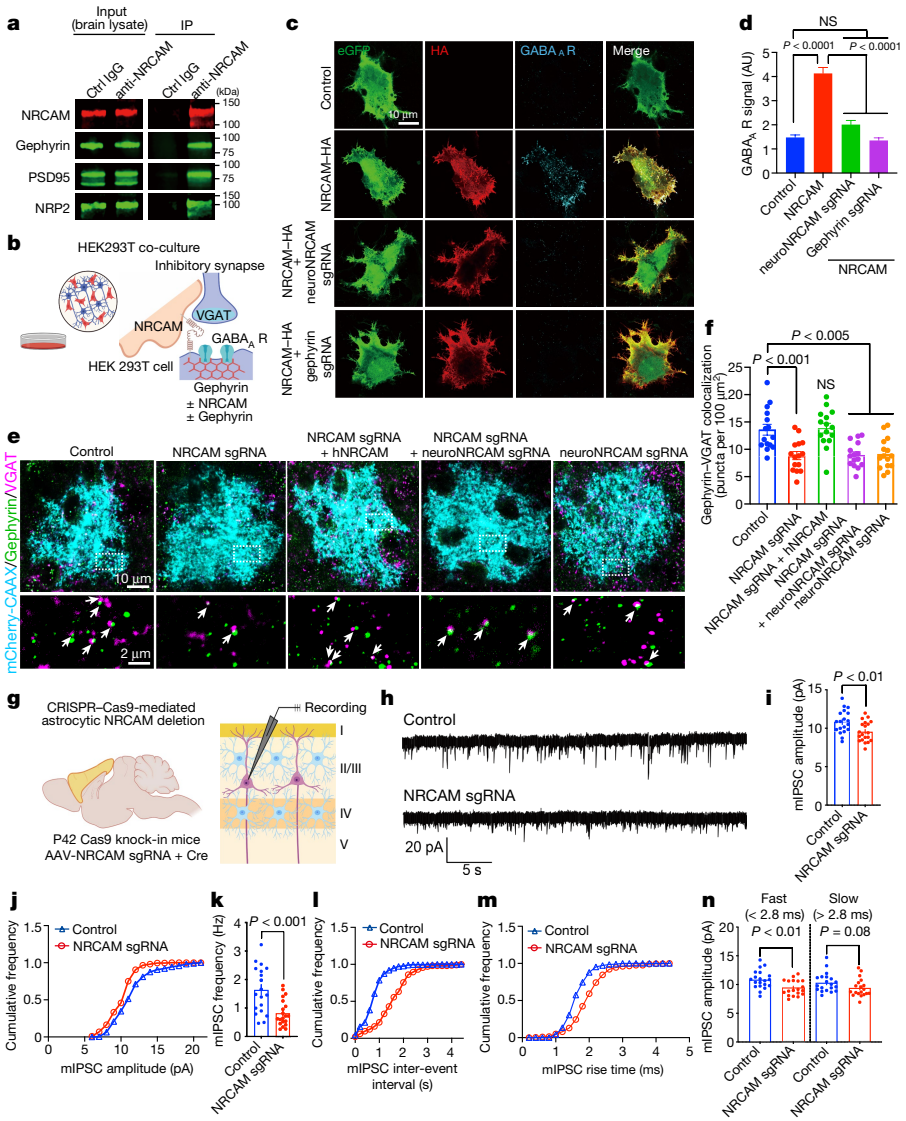

Fig. 4 | Astrocytic NRCAM controls inhibitory synaptic organization and function. a, Co-immunoprecipitation (IP) from cortical lysates of NRCAM with gephyrin, PSD95 and NRP2. **b**, Schematic of co-culture assay to identify effects of non-neuronal NRCAM–HA on inhibitory synaptic specializations. **c**, Images of NRCAM–HA coexpressed with eGFP in HEK 293T cells co-cultured with neurons depleted of NRCAM or gephyrin. **d**, Mean integrated intensity of $GABA_A$ receptor in contact with transfected HEK 293T cells counted from cells as in **c** (number of cells: $n = 418$ control, $n = 416$ NRCAM–HA, $n = 297$ neuroNRCAM sgRNA + NRCAM, $n = 356$ gephyrin sgRNA + NRCAM). **e**, Images of inhibitory synapses among NRCAM-deficient astrocytes. High magnification images (bottom) correspond to outlined areas (above), arrows indicate examples of colocalizing synaptic markers. **f**, Average number of inhibitory synaptic colocalized puncta within astrocyte territories from cells as in **e**. $n = 15$ cells per each condition from 3 mice. **g**, Schematic of electrophysiology experiments in L2/3 pyramidal neurons of V1 cortex. **h**, mIPSC traces from L2/3 pyramidal neurons following astrocyte treatment with control (empty sgRNA) or NRCAM sgRNA. **i**–**m**, mIPSC amplitude (**i**,**j**), frequency (**k**,**l**) and rise time (**m**) ($n = 20$ cells per condition from 4 mice). **n**, mIPSC amplitudes sorted by fast and slow rise times. In **d**, **f**, one-way ANOVA with Dunnett's multiple comparison; $n = 3$–6 biological repeats. In **i**, **k**, **n**, Student's paired *t*-test. Data are mean ± s.e.m.

the transcellular homophilic binding between astrocytic and neuronal NRCAMs is required for astrocyte morphogenesis, we targeted neuronal NRCAM using AAV-NrCAM sgRNA-hSynI-Cre. Depletion of NRCAM from only neurons or from both astrocytes and neurons enhanced astrocytic territory (at P14 but not at P42) and NIV (at both P14 and P42) to a similar degree to astrocyte-specific NRCAM deletion (Extended Data Fig. 7d–k). Together, these results indicate that homophilic binding between neuronal and astrocytic NRCAM restricts growth of astrocyte processes into the neuropil. This function of astrocytic NRCAM might be similar to its known role in promoting retraction of dendritic spines via semaphorin–plexin signalling in neurons[26]. Notably, SEMA7A and PLXNA4 were also detected in our proteomic analysis (Fig. 2b).

Astrocyte NRCAM modulates GABA synapses

Previous studies have shown that proper astrocyte morphogenesis is required for synaptic development, mediated through direct synaptic contact[9]. To determine whether astrocytic NRCAM is also important for astrocyte–synapse contacts, we used STED microscopy to analyse astrocyte-expressed NRCAM–HA with respect to excitatory and inhibitory synapses (Fig. 3a). We found that astrocytic NRCAM–HA closely associated with both synapse types (Fig. 3b). Then, to determine whether endogenous astrocytic NRCAM is localized at tripartite synaptic sites in vivo, we measured the distance from mCherry–CAAX-positive NRCAM puncta to excitatory ($VGLUT1^+$) and inhibitory ($VGAT^+$) presynapses (Fig. 3c) and compared this to localization of ezrin,

a protein known to be localized to perisynaptic astrocyte processes. The distances of NRCAM and ezrin puncta were a similar distance from presynapses[29,30] (Fig. 3d–f), demonstrating that astrocytic NRCAM is localized at astrocyte–synapse contacts in vivo.

To determine the effect of NRCAM loss on astrocyte–neuron contacts in vivo, we measured the distance between mCherry–CAAX-labelled astrocytic process and excitatory or inhibitory synapses (Fig. 3g). Deletion of astrocytic NRCAM did not alter the distance between astrocytic processes and excitatory pre- or postsynapses (Fig. 3h–j). However, the distance of astrocytic processes from inhibitory pre- and postsynapses was significantly increased (Fig. 3k–m). Furthermore, simultaneous deletion of both astrocytic and neuronal NRCAM, or of neuronal NRCAM alone, similarly disrupted contacts between astrocytes and inhibitory synapses (Fig. 3k–m).

The impairment of astrocyte–inhibitory synapse contacts due to loss of astrocytic NRCAM was rescued by expression of human NRCAM (Fig. 3k–m). This effect appeared to be directly related to NRCAM depletion as the levels of other proteins implicated in astrocyte–neuron interactions were unaffected (Extended Data Fig. 8a, b). Together, these results strongly support a model in which homophilic NRCAM interactions between astrocytes and neurons mediate adhesions between astrocytes and inhibitory synapses.

In previous studies, we identified neuronal NRCAM in the proteome of GABAergic postsynapses using iBioID with the inhibitory synapse organizer gephyrin as the bait[19]. Indeed, NRCAM co-immunoprecipitated with GFP–gephyrin when coexpressed in HEK 293T cells (Extended Data Fig. 8c), and endogenous NRCAM co-immunoprecipitated with gephyrin from brain lysate (Fig. 4a). The positive controls PSD95 and neuropilin-2 (NRP2)[26] were also detected in these co-immunoprecipitations, whereas negative control IgG did not precipitate gephyrin or positive-control proteins (Fig. 4a). These results indicate that NRCAM forms a complex with the neuronal GABAergic synaptic scaffolding protein gephyrin, and thus it may have a critical role in inhibitory synapse development in vivo.

To test whether NRCAM functions as an organizer for inhibitory synaptic specializations, we used an in vitro HEK 293T–neuron co-culture assay[31–33]. In this assay, consistent with previous studies, expression of NL2 in HEK 293T cells induced ectopic formation of excitatory ($VGLUT1^+$) and inhibitory ($VGAT^+$) presynapses[32,33] (Extended Data Fig. 8e–l). Similarly, expression of presynaptic neurexin-1β (NRX1β), induced excitatory ($HOMER1^+$) and inhibitory ($GABA_A$ receptor-positive) postsynapses around the HEK 293T cells[31,33] (Extended Data Fig. 8e–l). When NRCAM, NRCAM(ΔIG) or NRCAM(ΔECD) were expressed in HEK 293T cells co-cultured with neurons[31–33] (Extended Data Fig. 8b–l), the expression of NRCAM, but not the mutant NRCAMs, induced ectopic formation of inhibitory pre- and postsynaptic contacts (Extended Data Fig. 8e–h). NRCAM did not recruit excitatory synaptic specializations onto HEK 293T cells (Extended Data Fig. 8i–l). Of note, when NRCAM or gephyrin were deleted from neurons using specific sgRNAs (Fig. 4b), the ability of NRCAM-expressing HEK 293T cells to promote clustering of inhibitory post-synapses was abolished (Fig. 4c, d). Together, these data indicate that transcellular homophilic NRCAM interactions control the organization of inhibitory synaptic specializations via neuronal gephyrin.

NRCAM controls inhibition in vivo

Next, we examined the requirement of astrocytic NRCAM for excitatory or inhibitory synaptic structure and function in the mouse visual cortex. When we quantified the intracortical synapses of layer 2/3 neurons that are abundant in layer 1, we found that deletion of astrocytic NRCAM did not alter excitatory synapse number (Extended Data Fig. 9a, b). By contrast, deletion of astrocytic NRCAM significantly decreased inhibitory synapses in layer 2/3 of the mouse visual cortex (Fig. 4e, f). The effect of astrocytic NRCAM deletion on inhibitory synapse number was rescued by the expression of human NRCAM (Fig. 4e, f). The deletion of NRCAM from neurons alone or from both neurons and astrocytes significantly decreased inhibitory synapse numbers (Fig. 4e, f). This result further supports the idea that NRCAM bridges astrocytes and neurons via homophilic interactions to control inhibitory synapses.

To determine the functional consequences of deleting NRCAM from astrocytes, we performed whole-cell patch-clamp recordings of miniature excitatory postsynaptic currents (mEPSCs) and inhibitory postsynaptic currents (mIPSCs) of pyramidal neurons in layer 2/3 (Fig. 4g). The amplitude of mEPSCs was slightly decreased by the deletion of astrocytic NRCAM, but the frequency was not altered (Extended Data Fig. 9c–g). By contrast, both amplitude and frequency of mIPSCs were significantly decreased following NRCAM deletion compared with of controls (Fig. 4h–l). Inhibitory synapses that develop into pyramidal neurons are established by a heterologous population of interneurons, targeting either perisomatic or distal dendritic regions[34]. Owing to their juxtaposition to the recording electrode, somatic mIPSC events have much steeper rise kinetics than distal dendritic events and thus can distinguish between these two populations[35,36]. Notably, we saw an increase in the rise time of mIPSCs (Fig. 4m), which when separated by fast and slow events (fast being less than 2.8 ms and slow being over 2.8 ms)[36], showed a significant decrease of mIPSC amplitudes for the fast (somatic) (Fig. 4n) compared to slower (dendritic) rise time events. Thus, astrocytic NRCAM is probably important for proper somatic inhibitory synaptic development and function in vivo. It will be interesting to analyse how these effects modulate GABAergic networks, such as during visual cortical critical periods, in future studies.

Dissection of the in vivo chemical-affinity codes that organize the wiring of the brain in a cell-type-specific manner from tissue has remained a considerable challenge. In this study, we have developed an in vivo BioID approach for discovery of extracellular cell–cell contact proteomes (Extended Data Fig. 10, top). Our Split-TurboID approach differs from analogous methods in two ways: it can specify labelling of junctions between two genetically defined cell types, and it can be applied in vivo. Previously, synaptic cleft proteomics studies have been performed in vitro with split horseradish peroxidase-conjugated with neurexin and neuroligin[37,38] or with the synaptic adhesion molecule SynCAM1[39]. Both approaches have been highly successful, identifying excitatory and inhibitory synaptic cleft proteins in cultured cortical neurons. HRP-based labelling has the advantage of labelling synaptic clefts on a minute timescale in cultured cells or ex vivo[37,38,40]. However, a concern with this method is that the labelling requires H_2O_2, which is cytotoxic and difficult to use in living brain tissue while maintaining complex multicellular interactions of the neuropil. We designed TurboID-surface and Split-TurboID to overcome this issue. A different version of split-TurboID has been described recently for intracellular labelling between endoplasmic reticulum and mitochondria[41]. It will be interesting to test how this version performs when displayed extracellularly between cell types.

Astrocytes have been proposed to control inhibitory synapse formation via secreted proteins[42,43]; however, the presence of adhesion-based mechanisms through which astrocyte contacts control inhibitory synaptogenesis remain largely unknown. In this study we show that astrocytic and neuronal NRCAMs bridge these two cell types to foster inhibitory postsynaptic specializations via gephyrin. We propose that these postsynaptic specializations then recruit presynaptic neuronal partners, to direct the formation of tripartite inhibitory synapses (Extended Data Fig. 10, bottom). Loss of perisynaptic NRCAM interactions results in significant deficits of GABAergic transmission, with slight reductions in the amplitudes of glutamatergic responses. These reduced glutamatergic responses may be due to a well-documented homeostatic response to reduced inhibition[44,45], given the lack of effects of NRCAM on excitatory synapse formation in co-culture and depletion assays. Thus, our proteomic analysis reveals both a mechanism for how astrocytes modulate inhibitory synapses, and a protein

map to provide a basis for future studies of astrocyte–neuron signalling at synapses.

Online content

Any methods, additional references, Nature Research reporting summaries, source data, extended data, supplementary information, acknowledgements, peer review information; details of author contributions and competing interests; and statements of data and code availability are available at https://doi.org/10.1038/s41586-020-2926-0.

1. Yu, X., Nagai, J. & Khakh, B. S. Improved tools to study astrocytes. *Nat. Rev. Neurosci*. **21**, 121–138 (2020).
2. Lanjakornsiripan, D. et al. Layer-specific morphological and molecular differences in neocortical astrocytes and their dependence on neuronal layers. *Nat. Commun*. **9**, 1623 (2018).
3. Araque, A., Parpura, V., Sanzgiri, R. P. & Haydon, P. G. Tripartite synapses: glia, the unacknowledged partner. *Trends Neurosci*. **22**, 208–215 (1999).
4. Khakh, B. S. & Sofroniew, M. V. Diversity of astrocyte functions and phenotypes in neural circuits. *Nat. Neurosci*. **18**, 942–952 (2015).
5. Ma, Z., Stork, T., Bergles, D. E. & Freeman, M. R. Neuromodulators signal through astrocytes to alter neural circuit activity and behaviour. *Nature* **539**, 428–432 (2016).
6. Papouin, T., Dunphy, J., Tolman, M., Foley, J. C. & Haydon, P. G. Astrocytic control of synaptic function. *Phil. Trans. R. Soc. Lond. B* **372**, 20160154 (2017).
7. Panatier, A. et al. Astrocytes are endogenous regulators of basal transmission at central synapses. *Cell* **146**, 785–798 (2011).
8. Araque, A. et al. Gliotransmitters travel in time and space. *Neuron* **81**, 728–739 (2014).
9. Stogsdill, J. A. et al. Astrocytic neuroligins control astrocyte morphogenesis and synaptogenesis. *Nature* **551**, 192–197 (2017).
10. Stork, T., Sheehan, A., Tasdemir-Yilmaz, O. E. & Freeman, M. R. Neuron–glia interactions through the Heartless FGF receptor signaling pathway mediate morphogenesis of *Drosophila* astrocytes. *Neuron* **83**, 388–403 (2014).
11. Sloan, S. A. & Barres, B. A. Mechanisms of astrocyte development and their contributions to neurodevelopmental disorders. *Curr. Opin. Neurobiol*. **27**, 75–81 (2014).
12. Allen, N. J. & Lyons, D. A. Glia as architects of central nervous system formation and function. *Science* **362**, 181–185 (2018).
13. Branon, T. C. et al. Efficient proximity labeling in living cells and organisms with TurboID. *Nat. Biotechnol*. **36**, 880–887 (2018).
14. Schopp, I. M. et al. Split-BioID a conditional proteomics approach to monitor the composition of spatiotemporally defined protein complexes. *Nat. Commun*. **8**, 15690 (2017).
15. De Munter, S. et al. Split-BioID: a proximity biotinylation assay for dimerization-dependent protein interactions. *FEBS Lett*. **591**, 415–424 (2017).
16. Kinoshita, N. et al. Genetically encoded fluorescent indicator GRAPHIC delineates intercellular connections. *iScience* **15**, 28–38 (2019).
17. Lee, Y., Messing, A., Su, M. & Brenner, M. *GFAP* promoter elements required for region-specific and astrocyte-specific expression. *Glia* **56**, 481–493 (2008).
18. Chan, K. Y. et al. Engineered AAVs for efficient noninvasive gene delivery to the central and peripheral nervous systems. *Nat. Neurosci*. **20**, 1172–1179 (2017).
19. Uezu, A. et al. Identification of an elaborate complex mediating postsynaptic inhibition. *Science* **353**, 1123–1129 (2016).
20. Zhang, Y. et al. An RNA-sequencing transcriptome and splicing database of glia, neurons, and vascular cells of the cerebral cortex. *J. Neurosci*. **34**, 11929–11947 (2014).
21. Zhang, Y. et al. Purification and characterization of progenitor and mature human astrocytes reveals transcriptional and functional differences with mouse. *Neuron* **89**, 37–53 (2016).
22. Sakers, K. & Eroglu, C. Control of neural development and function by glial neuroligins. *Curr. Opin. Neurobiol*. **57**, 163–170 (2019).
23. Incontro, S., Asensio, C. S., Edwards, R. H. & Nicoll, R. A. Efficient, complete deletion of synaptic proteins using CRISPR. *Neuron* **83**, 1051–1057 (2014).
24. Custer, A. W. et al. The role of the ankyrin-binding protein NrCAM in node of Ranvier formation. *J. Neurosci*. **23**, 10032–10039 (2003).
25. Feinberg, K. et al. A glial signal consisting of gliomedin and NrCAM clusters axonal Na+ channels during the formation of nodes of Ranvier. *Neuron* **65**, 490–502 (2010).
26. Demyanenko, G. P. et al. Neural cell adhesion molecule NrCAM regulates Semaphorin 3F-induced dendritic spine remodeling. *J. Neurosci*. **34**, 11274–11287 (2014).
27. Mohan, V. et al. Temporal regulation of dendritic spines through NrCAM-Semaphorin3F receptor signaling in developing cortical pyramidal neurons. *Cereb. Cortex* **29**, 963–977 (2019).
28. Mauro, V. P., Krushel, L. A., Cunningham, B. A. & Edelman, G. M. Homophilic and heterophilic binding activities of Nr-CAM, a nervous system cell adhesion molecule. *J. Cell Biol*. **119**, 191–202 (1992).
29. Derouiche, A., Anlauf, E., Aumann, G., Mühlstädt, B. & Lavialle, M. Anatomical aspects of glia-synapse interaction: the perisynaptic glial sheath consists of a specialized astrocyte compartment. *J. Physiol. Paris* **96**, 177–182 (2002).
30. Lavialle, M. et al. Structural plasticity of perisynaptic astrocyte processes involves ezrin and metabotropic glutamate receptors. *Proc. Natl Acad. Sci. USA* **108**, 12915–12919 (2011).
31. Scheiffele, P., Fan, J., Choih, J., Fetter, R. & Serafini, T. Neuroligin expressed in nonneuronal cells triggers presynaptic development in contacting axons. *Cell* **101**, 657–669 (2000).
32. Graf, E. R., Zhang, X., Jin, S. X., Linhoff, M. W. & Craig, A. M. Neurexins induce differentiation of GABA and glutamate postsynaptic specializations via neuroligins. *Cell* **119**, 1013–1026 (2004).
33. Chih, B., Gollan, L. & Scheiffele, P. Alternative splicing controls selective trans-synaptic interactions of the neuroligin–neurexin complex. *Neuron* **51**, 171–178 (2006).
34. Tremblay, R., Lee, S. & Rudy, B. GABAergic interneurons in the neocortex: from cellular properties to circuits. *Neuron* **91**, 260–292 (2016).
35. Miles, R., Tóth, K., Gulyás, A. I., Hájos, N. & Freund, T. F. Differences between somatic and dendritic inhibition in the hippocampus. *Neuron* **16**, 815–823 (1996).
36. Wierenga, C. J. & Wadman, W. J. Miniature inhibitory postsynaptic currents in CA1 pyramidal neurons after kindling epileptogenesis. *J. Neurophysiol*. **82**, 1352–1362 (1999).
37. Martell, J. D. et al. A split horseradish peroxidase for the detection of intercellular protein-protein interactions and sensitive visualization of synapses. *Nat. Biotechnol*. **34**, 774–780 (2016).
38. Loh, K. H. et al. Proteomic analysis of unbounded cellular compartments: synaptic clefts. *Cell* **166**, 1295–1307 (2016).
39. Cijsouw, T. et al. Mapping the proteome of the synaptic cleft through proximity labeling reveals new cleft proteins. *Proteomes* **6**, E48 (2018).
40. Li, J. et al. Cell-surface proteomic profiling in the fly brain uncovers wiring regulators. *Cell* **180**, 373–386 (2020).
41. Cho, K. F. et al. Split-TurboID enables contact-dependent proximity labeling in cells. *Proc. Natl Acad. Sci. USA* **117**, 12143–12154 (2020).
42. Elmariah, S. B., Oh, E. J., Hughes, E. G. & Balice-Gordon, R. J. Astrocytes regulate inhibitory synapse formation via Trk-mediated modulation of postsynaptic $GABA_A$ receptors. *J. Neurosci*. **25**, 3638–3650 (2005).
43. Hughes, E. G., Elmariah, S. B. & Balice-Gordon, R. J. Astrocyte secreted proteins selectively increase hippocampal GABAergic axon length, branching, and synaptogenesis. *Mol. Cell. Neurosci*. **43**, 136–145 (2010).
44. Turrigiano, G. G., Leslie, K. R., Desai, N. S., Rutherford, L. C. & Nelson, S. B. Activity-dependent scaling of quantal amplitude in neocortical neurons. *Nature* **391**, 892–896 (1998).
45. O'Brien, R. J. et al. Activity-dependent modulation of synaptic AMPA receptor accumulation. *Neuron* **21**, 1067–1078 (1998).

Methods

No statistical methods were used to predetermine sample size. The experiments were not randomized. The investigators were blinded to allocation during experiments and outcome assessment.

Animals

All mice were housed (2–5 mice per cage) at the Division of Laboratory Animal Resources facilities at Duke University. All procedures were conducted with a protocol approved by the Duke University Institutional Animal Care and Use Committee in accordance with US National Institutes of Health guidelines. All mice were kept under typical day:night conditions of 12 h cycles. CD1 (022, Charles River), Cas9 (028239) and Ai14 (007914) mice were purchased from Jackson laboratory. Both males and females were used, ages ranged from P0 to P42.

Plasmid construction

pZac2.1-GfaABC1D-Lck-GCaMP6f was a gift from B. Khakh (UCLA) (Addgene plasmid #52924). pcDNA3-V5-TurboID-NES was a gift from A. Ting (Stanford) (Addgene plasmid #107169). GRAPHIC was obtained as previously described[16]. TurboID was subcloned into pZac2.1-GfaABC1D vector. The split sites of Split 1-TurboID and Split 2-TurboID were at the 256/257 and 140/141 amino acid position, respectively. The N-TurboID and C-TurboID fragments were subcloned into AAV-hSynI and pZac2.1-GfaABC1D vector, respectively. AAV-hSynI-EGFP and pZac2.1-GfaABC1D-mCherry-CAAX were previously described[9,19]. GfaABC1D was amplified and subcloned into AAV-U6-sg-Cre vectors. The sgRNA sequences used were as follows: *Tenm2*, 5′- ATCTGGAATAATGGATGTAAAGG-3′; *Tenm4*, 5′- GCCAGAGGCCATGGACGTGAAGG-3′; *Nrcam*, 5′- GTGCCAGA TGATCAGCGCGCTGG-3′. The gephyrin sgRNA was obtained as previously described[19]. The cDNA encoding human NRCAM (Gene ID4897, Dharmacon) was amplified and subcloned into AAV-Ef1α, AAV-hSynI, pZac2.1-GfaABC1D vector. The fragments encoding human NRCAM mutants (hNrCAM-ΔIg and hNrCAM-ΔECD) were subcloned into AAV-Ef1α and pZac2.1-GfaABC1D vector. pCAG-HA-Nrxn1beta AS4(-) and pNICE-NL2(-) were gifts from P. Scheiffele (University of Basel) (Addgene plasmid #59409 and #15246, respectively). pEGFP-gephyrin and pcDNA-PSD95-GFP were previously described[19]. All constructs were confirmed by DNA sequencing. All primers are shown in Supplementary Table 4.

Antibodies

The following antibodies were used: monoclonal anti-V5 (ThermoFisher, R960-25, immunoblot (IB) 1:1,000, immunofluorescence (IF) 1:500, immunohistochemistry (IHC) 1:500), rat anti-HA (Sigma, 12158167001, IB 1:1,000, IF 1:500, IHC 1:200), mouse anti-HA (Biolegend, MMS-101P, IB 1:1,000), chicken anti-GFP (Abcam, ab13970, IB 1:1,000, IF 1:1,000, IHC 1:1,000), rabbit anti-mCherry (Abcam, ab167453, IF 1:500, IHC 1:500), rabbit anti-PSD95 (Life Techonologies, 51-6900, IHC 1:200), mouse anti-PSD95 (ThermoFisher, 7E3, IB 1:1,000), guinea pig anti-VGLUT1 (Synaptic Systems, 135-304, IF 1:1,000, IHC 1:1,000), rabbit anti-gephyrin (Synaptic Systems, 147-002, IF 1:1,000, IHC 1:500), mouse anti-gephyrin (Synaptic Systems, 147-011, IB 1:1000, IF 1:300), guinea pig anti-VGAT (Synaptic System, 131-004, IF 1:1,000, IHC 1:500), rabbit anti-NL2 (Synaptic System, 129-202, IB 1:500), rabbit anti-NRCAM (Abcam, ab24344, IB 1:1,000, IHC 1:200), rabbit anti-HOMER1 (Synaptic Systems, 160002, IF 1:2,000), rabbit anti-GABA-A receptor β2 (Synaptic Systems, 224-803, IF 1:1,000), goat anti-neuropilin-2 (R & D Systems, AF567, IB 1:500), rat anti-tdTomato (Kerafast, EST203, IHC 1:1,000), rat anti-tubulin (Santa Cruz, sc-53029, IB 1:1,000), rabbit anti-Ezrin (Cell Signaling, 3142, IHC 1:200), rabbit anti-EAAT2 (GLT1) (Alamone, AGC-022, IB 1:1,000), rabbit anti-KIR4.1 (Alamone, APC-035, IB 1:500), rabbit anti-NL3 (Novus, NBP1-90080, IB 1:500), Alexa Fluor 488 Goat anti-Mouse (ThermoFisher, A32723), Alexa Fluor 488 Goat anti-Rabbit (ThermoFisher, A-11034), Alexa Fluor 488 Goat anti-Guinea pig (ThermoFisher, A11073), Alexa Fluor 488 Goat anti-Chicken (ThermoFisher, A-11006), Oregon Green 488 Goat anti-Rabbit (ThermoFisher, O-11038), Alexa Fluor 555 Goat anti-Rabbit (ThermoFisher, A21428), Alexa Fluor 568 Goat anti-Rat (ThermoFisher, A-11077), Alexa Fluor 594 Streptavidin (ThermoFisher, S11227), Alexa Fluor 647 Donkey anti-rabbit (ThermoFisher, A31573), Alexa Fluor 647 Goat anti-Chicken (ThermoFisher, A-21449), Alexa Fluor 647 Donkey anti-Guinea pig (Jackson ImmunoResearch, 706-605-148), Alexa Fluor 647 Streptavidin (ThermoFisher, S21374), Atto647N anti-Mouse (Sigma, 50185), Atto647N anti-rabbit (Sigma, 40839), Donkey anti-Goat IRDye 800CW (LI-COR, 926-32214), Goat anti-rat IRDye 800CW (LI-COR, 925-32219) and Goat anti-Mouse IRDye 680RD (LI-COR, 925-6818).

AAV production

AAVs were produced as previously described[19,46]. In brief, HEK 293T cells (obtained from ATCC, CRL-11268; short tandem repeat confirmed and mycoplasma negative) were transfected with pAd-DELTA F6, serotype plasmid AAV PHP.eB and AAV plasmid. After 72 h, the cells were lysed in 15 mM NaCl, 5 mM Tris-HCl, pH 8.5, and incubated with 50 U ml^{-1} benzonase for 30 min at 37 °C. The cell lysate was then centrifuged at 4,500 rpm for 30 min at 4 °C, and the supernatant containing AAV was added to the top of an iodixanol gradient (15%, 25%, 40% and 60% iodixanol solution, top to bottom) and centrifuged using a Beckman Ti-70 rotor, spun at 67,000 rpm for 1 h. The viral solution extracted from the virus layer (between the 40% and 60% iodixanol layers) with a 24-gauge needle and 5-ml syringe, and concentrated with a 100-kDa filter. Viral titres were measured by quantitative PCR using a linearized genome plasmid as a standard[47]. For small-scale AAV supernatant, HEK 293T cells were transfected pAd-DELTA F6, serotype plasmid AAV PHP.eB or AAV2/1 and AAV plasmid. After 72 h, the AAV-containing supernatant medium was collected and filtered with a 0.45-μm cellulose acetate Spin-X centrifuge tube filter (Costar 8162).

Primary neuronal, astrocytic and HEK 293T cell cultures

Cortical neurons and astrocytes were prepared from P1 mouse pups. These cells were seeded on coverslips or dishes coated with poly-L-lysine (Sigma) and cultured in neurobasal medium A (Invitrogen) supplemented with B-27 (Invitrogen) and 1 mM GlutaMAX (Invitrogen). Mouse cortical astrocytes were prepared as previously described[9]. P0-3 mouse cortices were microdissected and papain digested followed by trituration in low and high ovomucoid solutions. Cells were passed through a 20-μm mesh filter, resuspended in astrocyte growth medium (AGM; DMEM (Gibco 11960), 10% FBS, 10 μM, hydrocortisone, 100 U ml^{-1} penicillin/streptomycin, 2 mM L-glutamine, 5 μg ml^{-1} Insulin, 1 mM sodium pyruvate, 5 μg ml^{-1} *N*-acetyl-L-cysteine) and 30 million cells were plated on 75-mm^2 flasks (non-ventilated cap) coated with poly-D-lysine. Flasks containing cells were incubated at 37 °C in 10% CO_2. On day in vitro (DIV) 3, AGM was removed and replaced with DPBS. Flasks were then shaken vigorously by hand for 10–15 s until only the adherent monolayer of astroglia remained. DPBS was then replaced with fresh AGM. On DIV 4, the medium was supplemented with AraC protein for 3 days to eliminate fast dividing cells, and astrocytes were treated with AAVs. On DIV 7, astrocytes were passaged into 6-well dishes (400,000 cells per well) and half the medium was replaced every 2–3 days. On DIV 14, astrocytes were collected for immunoblotting analysis. HEK 293T (obtained from ATCC, CRL-11268; short tandem repeat confirmed and mycoplasma negative) cells were maintained in DMEM (Gibco) supplemented with 10% FBS (Gibco) and 100 U ml^{-1} penicillin/streptomycin. Cell lines were incubated at 37 °C in 5% CO_2. Cells were regularly passaged every three days.

Immunostaining and imaging analysis

Cultured neurons and astrocytes were infected with small-scale AAVs at DIV 14. After 3 days, these cells were treated with 500 μM biotin for 6 h.

Neurons and astrocytes were fixed at indicated time points in 4% PFA, 4% sucrose for 20 min at room temperature. They were permeabilized with 0.1% Triton-X 100 and 10% normal goat serum (NGS) for 30 min at room temperature. Samples were then incubated for overnight at 4 °C with primary antibodies followed by Alexa Fluor 488-, Alexa Fluor 555 or Alexa 647-conjugated secondary antibodies diluted in PBS containing 0.01% Triton X-100 and 10% NGS for 2 h at room temperature. The neuron and HEK 293T cells mixed-culture assay was performed as previously described[32,33]. In brief, HEK 293T cells were transfected using Lipofectamine 2000 according to the manufacturer's instructions. After 20 h, transfected HEK 293T cells were seeded on cultured neurons at DIV 14. Fluorescence images were acquired with Zeiss Imager M2 upright microscope equipped with an Apotome module, Zeiss 710, Zeiss 780 or Zeiss 880 confocal microscopes using the Zen Software or a stimulated emission depletion (STED) super resolution microscope (TCS SP8 STED, Lecia Microsystems) using the Leica Application Suite (LAS) software. The individual acquiring the images was always blinded to the experiment. Images were quantified and post-processed using FIJI.

Immunohistochemistry and imaging analysis

Immunohistochemistry was performed as previously described[48,49]. In brief, brains were fixed in 4% PFA, 4% sucrose, and coronally or sagittally sectioned with a cryostat (Leica Microsystems) at a thickness of 40 µm or 100 µm. The slices were incubated with primary antibodies diluted in PBS containing 0.1% Triton X-100 and 10% NGS at 4 °C for 2 days followed by Alexa Fluor 488- or Alexa Fluor 555- or Alexa 647-conjugated secondary antibodies diluted in PBS containing 0.1% Triton X-100 and 10% NGS for 2 h at room temperature. The nuclei were visualized by staining with DAPI.

Astrocyte morphology was analysed as previously described[9]. For the astrocyte territory volume analysis, entire astrocytes expressing mCherry–CAAX in 100 µm-thick floating sections were imaged using a 63× objective with 1× optical zoom images on the Zeiss 780 upright confocal microscope (Zen Software) and processed with Imaris software. The fluorescence signal from each astrocyte was reconstructed using the surface tool. The intersecting nodes of the surface render (vertices) were identified using the Matlab extension 'Visualize Surface Spots'. The Matlab Xtension 'Convex hull' identified the most terminal vertices (outside edges of the 3D surface render) and created an additional surface render to connect these terminal vertices by the shortest distance possible. Thus, a surface render of the outer rim (that is, territory) of each astrocyte was formed. The volume of each territory was measured in Imaris and recorded. Astrocyte territory sizes between experimental conditions were statistically analysed using one-way ANOVA followed by Fisher's least-squares difference (LSD) post hoc test when necessary. The individual analysing the images was always blinded to the experimental conditions. For the NIV analysis, astrocytes expressing mCherry–CAAX were imaged by 63× plus 2× optical zoom high magnification on Zeiss 710 confocal microscope. The images were uploaded into Imaris Bitplane software for 3D reconstructions. We chose at least three regions of interest (ROIs) measuring 200 pixels × 200 pixels × 20 pixels from each astrocyte that were devoid of the soma and large branches. ROIs were reconstructed using the surface tool in Imaris. NIV was calculated in Imaris and statistically analysed using a one-way ANOVA followed by a Fisher's LSD post hoc test. Images were analysed blinded to the experimental conditions.

Analysis of synaptic number

Synaptic number was analysed as previously described[9]. In brief, P42 control and experimental tissue sections were stained with an antibody against mCherry, biotinylated proteins and the following antibodies against pre- and postsynaptic protein pairs: VGLUT1 and PSD95 (makers of excitatory synapses) and VGAT and gephyrin (markers of inhibitory synapses). Five-micrometre-thick *Z*-stacks of 15 optical sections of astrocytes expressing mCherry–CAAX were imaged by 63× plus 1× optical zoom high magnification on Zeiss 780 confocal microscope (Zen Software). Synapse number quantification by colocalization takes advantage of the fact that pre- and postsynaptic proteins appear colocalized at synaptic junctions due to their close proximity. Each *Z*-stack was converted into 5 maximum projection images by condensing three consecutive optical sections using ImageJ. The number of colocalized synaptic puncta of excitatory intracortical (VGLUT1–PSD95), and inhibitory (VGAT–gephyrin) were obtained using the ImageJ plugin Puncta Analyzer[50] (B. Wark, available upon request from cagla.eroglu@dm.duke.edu). For each image, colocalized synaptic puncta were quantified within astrocytes from ROIs of 100 μm^2 area that were focused away from regions with neuronal cell bodies (areas lacking synaptic puncta). Statistical analysis of the synaptic staining was performed with a one-way ANOVA followed by a post hoc Fisher's LSD test when necessary. Images were analysed blinded to the experimental conditions.

Analysis of synaptic distance

Synaptic distance was analysed with super-resolution imaging as previously described[51]. In brief, P42 control and experimental tissue sections were stained with an antibody against mCherry, NRCAM, Ezrin and synaptic makers (VGLUT1, PSD95, VGAT and gephyrin). Optical sections of astrocytes expressing mCherry–CAAX were imaged by 93× plus 5× optical zoom high magnification on a STED microscope (TCS SP8 STED, Lecia Microsystems). The distance was measured as the distance between the peak positions of the two distributions of localization points using the Leica Application Suite (LAS) software. Statistical analysis was performed with a Student's *t*-test or one-way ANOVA followed by a post hoc Fisher's LSD test when necessary. Images were analysed blinded to the experimental conditions.

In vivo TurboID protein purification

In vivo TurboID experiments were performed as previously described[19,46], with some modifications. Each AAV-TurboID probe virus was retro-orbitally injected into CD1 juvenile mouse brain (P21). Three weeks after viral injection, biotin was subcutaneously injected at 24 mg kg^{-1} for 7 consecutive days to increase the biotinylation efficiency. For each TurboID probe, 4–10 mice were used for biotinylated protein purification. Each purification was performed independently at least three times. Each cortex was lysed in 50 mM Tris/HCl, pH 7.5; 150 mM NaCl; 1 mM EDTA; protease inhibitor mixture (cOmplete Mini EDTA-free, Roche); and phosphatase inhibitor mixture (PhosSTOP, Roche). The lysed samples were added to an equal volume of 50 mM Tris-HCl, pH 7.5, 150 mM NaCl, 1 mM EDTA, 0.4% SDS, 2% TritonX-100, 2% deocycholate, protease inhibitor mixture and phosphatase inhibitor mixture, and then sonicated and centrifuged at 15,000*g* for 10 min. Supernatant was further ultracentrifuged at 100,000*g* for 30 min at 4 °C (Beckman TLA-100 ultracentrifuge, TLA-55 rotor). SDS was added to the cleared supernatant to a final concentration of 1% and heated at 45 °C for 45 min. The sample was cooled on ice and incubated with Pierce High Capacity NeutrAvidin Agarose (ThermoFisher) at 4 °C overnight. Beads were washed twice with 2% SDS; twice with 1% TritonX-100, 1% deoxycholate, 25 mM LiCl; twice with 1 M NaCl and 5 times with 50 mM ammonium bicarbonate. Biotinylated proteins were eluted in 125 mM Tris-HCl, pH6.8, 4% SDS, 0.2% β-mercaptoethanol, 20% glycerol and 3 mM biotin at 60 °C for 15 min.

Quantitative LC–MS/MS analysis

Samples were spiked with either a total of 120 or 240 fmol of casein and reduced with 10 mM dithiolthreitol for 30 min at 80 °C and alkylated with 20 mM iodoacetamide for 45 min at room temperature, then supplemented with a final concentration of 1.2% phosphoric acid and 328 µl of S-Trap (Protifi) binding buffer (90% methanol, 100 mM triethylammonium bicarbonate (TEAB)). Proteins were trapped on the S-Trap, digested using 20 ng μl^{-1} sequencing grade trypsin (Promega) for

1 h at 47 °C, and eluted using 50 mM TEAB, followed by 0.2% formic acid (FA), and lastly using 50% acetonitrile, 0.2% FA. All samples were then lyophilized to dryness and resuspended in 12 µl 1% trifluoroacetic acid, 2% acetonitrile containing 12.5 fmol µl^{-1} yeast alcohol dehydrogenase. From each sample, 3 µl was removed to create a QC pool sample which was run periodically throughout the acquisition period.

Quantitative LC–MS/MS was performed on 2 µl of each sample, using a nanoAcquity UPLC system (Waters Corp) coupled to a Thermo Orbitrap Fusion Lumos high resolution accurate mass tandem mass spectrometer (Thermo) via a nanoelectrospray ionization source. In brief, the sample was first trapped on a Symmetry C18 20 mm × 180 µm trapping column (5 µl min^{-1} at 99.9/0.1 v/v water/acetonitrile), after which the analytical separation was performed using a 1.8 µm Acquity HSS T3 C18 75 µm × 250 mm column (Waters) with a 90-min linear gradient of 5–30% acetonitrile with 0.1% formic acid at a flow rate of 400 nl min^{-1} with a column temperature of 55 °C. Data collection on the Fusion Lumos mass spectrometer was performed in a data-dependent acquisition (DDA) mode of acquisition with r = 120,000 (at m/z 200) full MS scan from m/z 375 to 1,500 with a target AGC value of 2×10^5 ions. MS/MS scans were acquired at rapid scan rate in the linear ion trap with an AGC target of 5×10^3 ions and a max injection time of 100 ms. The total cycle time for MS and MS/MS scans was 2 s. A 20 s dynamic exclusion was employed to increase depth of coverage.

Following data collection, data were imported into Proteome Discoverer 2.2 (Thermo Scientific), and individual LC–MS .raw files were aligned on the basis of the accurate mass and retention time of detected ions ('features') using the Minora Feature Detector algorithm in Proteome Discoverer. Relative peptide abundance was calculated based on peak intensities following integration of selected ion chromatograms of the aligned features across all runs. The MS/MS data was searched against a SwissProt *Mus musculus* database (downloaded in Apr 2018) containing an equal number of reversed-sequence 'decoys' for false discovery rate determination. Mascot Distiller and Mascot Server (v.2.5, Matrix Sciences) were used to produce fragment ion spectra and to perform the database searches using full trypsin enzyme rules with 5 ppm precursor and 0.8 Da product ion match tolerances. Database search parameters included fixed modification on cysteine (carbamidomethyl) and variable modifications on methionine (oxidation) and asparagine and glutamine (deamidation). Peptide Validator and Protein FDR Validator nodes in Proteome Discoverer were used to annotate the data at a maximum 1% protein false discovery rate.

Split-TurboID protein network

Split-TuboID and TurboID-surface protein networks were performed as previously described[19,46] with modifications. Network figures were created using Cytoscape (v.3.7), with nodes corresponding to the gene name (multiple isoforms of proteins were collapsed into one node based on gene nomenclature) for proteins identified in the proteomic analysis. The known protein–protein interaction networks were provided by Strings, HitPredict, HPRD, BioGrid and APID database. A non-redundant list of protein–protein interactions was assembled using the MGI database, GeneCard and UniProt (Supplementary Tables 5–6). In all networks, node size is proportional to fold enrichment over soluble TurboID alone. However, the bait (Split-TurboID and TurboID-surface) node sizes were set manually. Clustergrams were created by manual inspection on the basis of Uniprot and GeneCard database annotation as previously described[19,46].

Immunoprecipitation and immunoblotting

HEK 293T cells were transfected with Lipofectamine 2000 according to the manufacturer's instructions. After 20 h, transfected HEK 293T cells were lysed in 25 mM HEPES, pH 7.5, 150 mM NaCl, 1 mM EDTA, 1% NP-40, protease inhibitor mixture and phosphatase inhibitor mixture. The cell lysate, which was obtained by centrifugation at 15,000g for 15 min at 4 °C, was incubated with GFP-Trap Agarose beads (Chromotek) at 4 °C overnight. For the protein expression assay from cultured astrocytes, the cell was lysed in 25 mM Tris, pH 7.4, 150 mM NaCl, 1 mM $CaCl_2$, 1 mM $MgCl_2$, 0.5% NP-40 and protease inhibitor mixture. The lysed samples were centrifuged at 15,000g for 5 min at 4 °C. For the endogenous NRCAM binding assay, juvenile mouse cortex (P42) was lysed in 25 mM HEPES, pH 7.5; 150 mM NaCl; 1 mM EDTA; 1% NP-40; protease inhibitor mixture; and phosphatase inhibitor mixture. The lysed samples were centrifuged at 15,000g for 10 min at 4 °C. Supernatant was pre-cleared with at 4 °C for 30 min with Protein G Sepharose beads (Millipore). NRCAM was immunoprecipitated with anti-NRCAM antibody followed by Protein G Sepharose beads overnight at 4 °C. SDS–PAGE and immunoblotting were performed as previously described[48,49]. The data were obtained with Odyssey Software v.4. Full gel images are shown in Supplementary Fig. 1.

Electrophysiological analysis

For whole-cell patch clamp recordings, P42–48 mice were decapitated under deep isoflurane anaesthesia. Brains were removed and 300-µm sagittal slices were prepared in ice cold, oxygenated cutting solution containing (in mM) 85 NaCl, 3 KCl, 1.3 $MgSO_4 \cdot 7H_2O$, 1.25 $NaH_2PO_4 \cdot H_2O$, 26 $NaHCO_3$, 25 dextrose, 2.5 $CaCl_2$, and 75 sucrose at ~320 mOsm l^{-1}, with a vibratome (Leica VT 1000S). Slices were recovered for 30 min at 31.5 °C in 95% O_2, 5% CO_2 bubbled artificial cerebrospinal fluid (ACSF) (containing (in mM) 124 NaCl, 3 KCl, 1.3 $MgSO_4 \cdot 7H_2O$, 1.25 $NaH_2PO_4 \cdot H_2O$, 26 $NaHCO_3$, 10 dextrose, 2.5 $CaCl_2$ at ~310 mOsm l^{-1}) and then at room temperature for at least 1 h. Slices were superfused with oxygenated ACSF at room temperature. To isolate mIPSCs, 50 µm D-APV, 10 µm NBQX and 0.5 µm TTX was added to ACSF. To isolate mEPSCs, 0.5 µm picrotoxin and 0.5 µm tetrodotoxin (TTX) was added to ACSF. V1 cells were visually identified under Zeiss Axio Examiner.D1 microscope with 20× dipping objective and IR-1000 camera (DAGE-MTI) using an IR bandpass filter. Cortical cells in layer 2/3 were patched using glass pipettes (4–7 MΩ resistance) made from borosilicate glass capillaries (Sutter Instrument) using a P-97 puller (Sutter Instrument). Pipettes were filled with internal solution containing: (in mM) 135 $CsMeSO_3$, 8 NaCl, 10 HEPES, 0.3 EGTA, 10 Na_2-phosphocreatine, 4 MgATP, 0.3 Na2GTP, 5 TEA-Cl, 5 QX-314 at ~290 mOsm l^{-1}. Miniature post-synaptic currents were measured at −70 mV. Series resistance was monitored throughout all recordings and only recordings that remained stable over the recording period (≤30 MΩ resistance and <20% change in resistance) were included. Data were recorded using a Multiclamp 700B amplified (Molecular Devices), digitized at 50 kHz using a Digidata 1550 digitizer (Molecular Devices), and low-pass filtered at 1kHz. All data were acquired using pClamp software and analysed in Clampfit (Molecular Devices) including only events larger than 5 pA. Events were initially identified using a custom-made template and manually assessed for inclusion with the template search function. Rise time was defined as the time from 10–90% of the peak. All chemicals were purchased from Sigma-Aldrich or Tocris. Experiments were performed blinded to the condition.

Statistical analysis

Data are expressed as the mean ± s.e.m. Statistical analyses were performed with GraphPad Prism version 6 (GraphPad Software). We compared independent sample means using t-tests and one-way ANOVAs as appropriate. Statistically significant F values detected in the ANOVAs were followed by alpha-adjusted post hoc tests (Tukey's honestly significant difference). We confirmed necessary parametric test assumptions using the Shapiro–Wilk test (normality) and Levene's test (error variance homogeneity). $P < 0.001$, $P < 0.01$ and $P < 0.05$ were considered to indicate statistical significance. Sample size for each experiment is indicated in the figure legend for each experiment. Sample sizes were determined based on previous

experience for each experiment to yield high power to detect specific effects. No statistical methods were used to predetermine sample size. All results of the statistical analysis are shown in Supplementary Table 7.

Reporting summary

Further information on research design is available in the Nature Research Reporting Summary linked to this paper.

Data availability

Proteomics data are available in the MassIVE database under accession MSV000085821. The data that support the findings of this study are available from the corresponding author upon reasonable request.

46. Spence, E. F. et al. In vivo proximity proteomics of nascent synapses reveals a novel regulator of cytoskeleton-mediated synaptic maturation. *Nat. Commun.* **10**, 386 (2019).
47. Shin, J. H., Yue, Y. & Duan, D. Recombinant adeno-associated viral vector production and purification. *Methods Mol. Biol.* **798**, 267–284 (2012).
48. Takano, T. et al. LMTK1 regulates dendritic formation by regulating movement of Rab11A-positive endosomes. *Mol. Biol. Cell* **25**, 1755–1768 (2014).
49. Takano, T. et al. Discovery of long-range inhibitory signaling to ensure single axon formation. *Nat. Commun.* **8**, 33 (2017).
50. Ippolito, D. M, Eroglu, C. Quantifying synapses: an immunocytochemistry-based assay to quantify synapse number. *J. Vis. Exp.* **16**, 2270 (2010).
51. Dani, A., Huang, B., Bergan, J., Dulac, C. & Zhuang, X. Superresolution imaging of chemical synapses in the brain. *Neuron* **68**, 843–856 (2010).

Acknowledgements We thank H. Katsura for modifying the promoter of the surface and split TurboID plasmids for HEK 293T cell expression, and B. Duncan for technical support. This work was supported by Brain initiative RO1DA047258 from NIH (S.H.S. and C.E.), R01MH113280 from NIH (P.F.M.), Kahn Neurotechnology Award (S.H.S. and C.E.), a Grant-in-Aid for JSPS Fellows (PD) 20153173 from the Japan Society for the Promotion of Science (T.T.), The Uehara memorial Foundation (T.T.), and National Institute of Mental Health Fellowship F30MH117851 (J.L.C).

Author contributions T.T., C.E. and S.H.S. designed the study. T.T., J.T.W., A.P., C.E. and S.H.S. wrote the manuscript. T.T., J.T.W., A.U. and E.J.S. performed in vivo BioID-proteomics analysis. T.T., J.T.W., J.L.C., T.S. and P.F.M. produced the constructs. T.T., J.T.W. and K.T.B. performed imaging analysis and the morphological analysis of the astrocytes. A.P. performed electrophysiological analysis. T.T. and K.T.B. performed the biological experiments. All authors discussed the results and commented on the manuscript text.

Competing interests The authors declare no competing interests.

Additional information
Supplementary information is available for this paper at https://doi.org/10.1038/s41586-020-2926-0.
Correspondence and requests for materials should be addressed to T.T., C.E. or S.H.S.
Peer review information *Nature* thanks Thomas Biederer, Peter Scheiffele and the other, anonymous, reviewer(s) for their contribution to the peer review of this work.
Reprints and permissions information is available at http://www.nature.com/reprints.

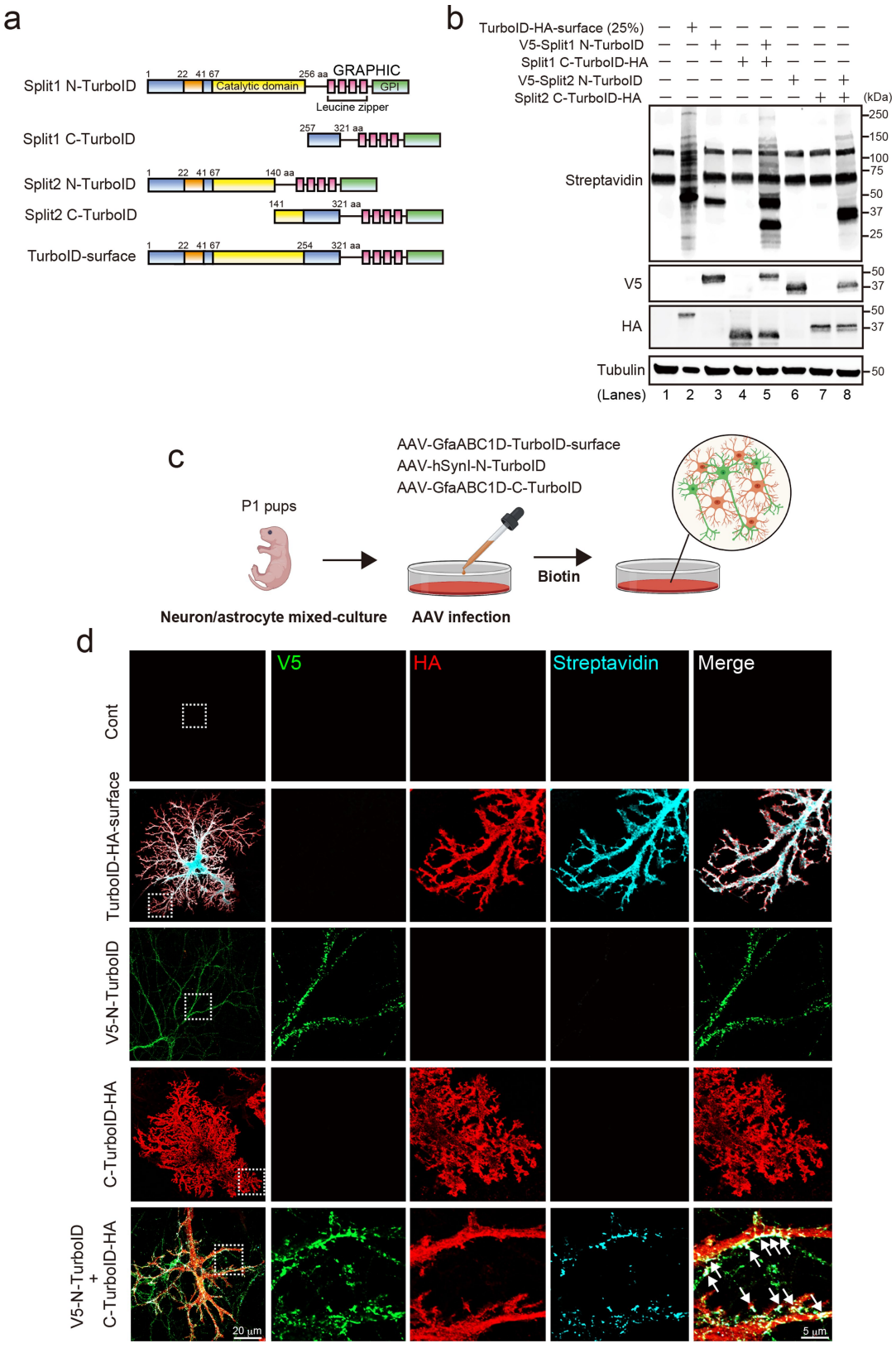

Extended Data Fig. 1 | The reconstituted activity of Split-TurboID in neurons and astrocytes in vitro. a, Schematics of constructs tested. **b**, Immunoblot analysis of construct expression and biotinylation activity. **c**, Schematic of neuron-astrocyte mixed-culture assay for Split-TurboID with cell-type-specific AAVs in vitro. **d**, Cultured neurons and astrocytes were infected with AAV1/2-GfaABC1D-TurboID-HA-surface, AAV1/2-hSynI-V5-N-TurboID and/or AAV1/2-GfaABC1D-C-TurboID-HA. Representative images of neuron and astrocyte at DIV14 after the treatment of 500 μM biotin for 6h are shown. $n = 3$ biological repeats.

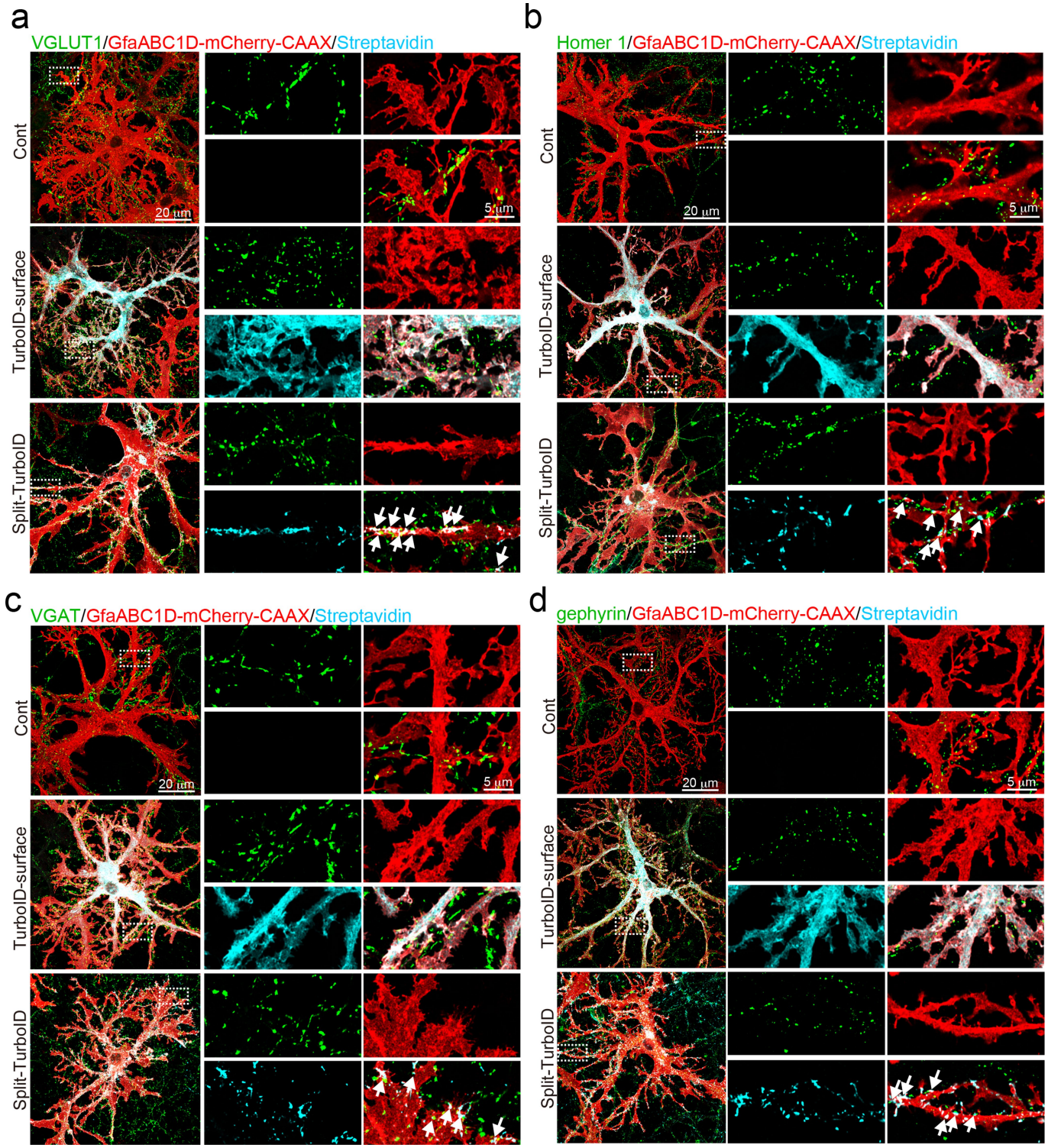

Extended Data Fig. 2 | Split-TurboID maps excitatory and inhibitory perisynaptic proteins. a–**d**, Representative images demonstrating that proteins biotinylated by astrocytic TurboID-surface or Split-TurboID (cyan) are adjacent to excitatory presynaptic marker VGLUT1 (**a**), postsynaptic marker HOMER1 (**b**), inhibitory presynaptic marker VGAT (**c**), and postsynaptic marker gephyrin (**d**). Astrocytes were visualized with GfaABC1D-mCherry-CAAX. $n = 3$ biological repeats.

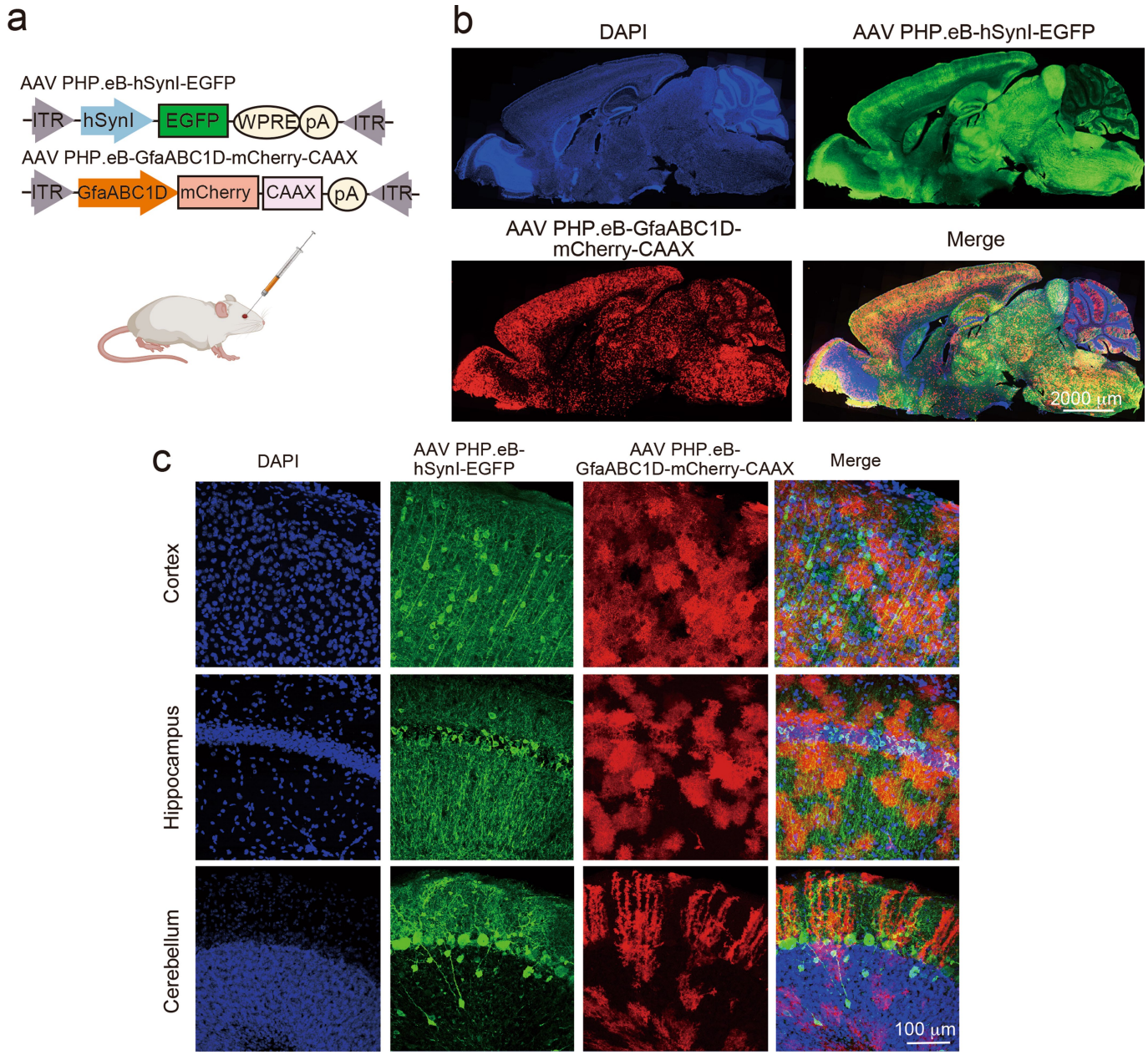

Extended Data Fig. 3 | Brain-wide transduction of astrocytes and neurons. **a**, Schematic of AAV PHP.eB viruses for neuronal-EGFP or astrocyte-mCherry-CAAX and retro-orbital injection. **b**, Sagittal section of mouse brain showing expression throughout the cortex and other structures. **c**, Representative image from cortex, hippocampus or cerebellum showing high coverage of neuronal and astrocytic expression.

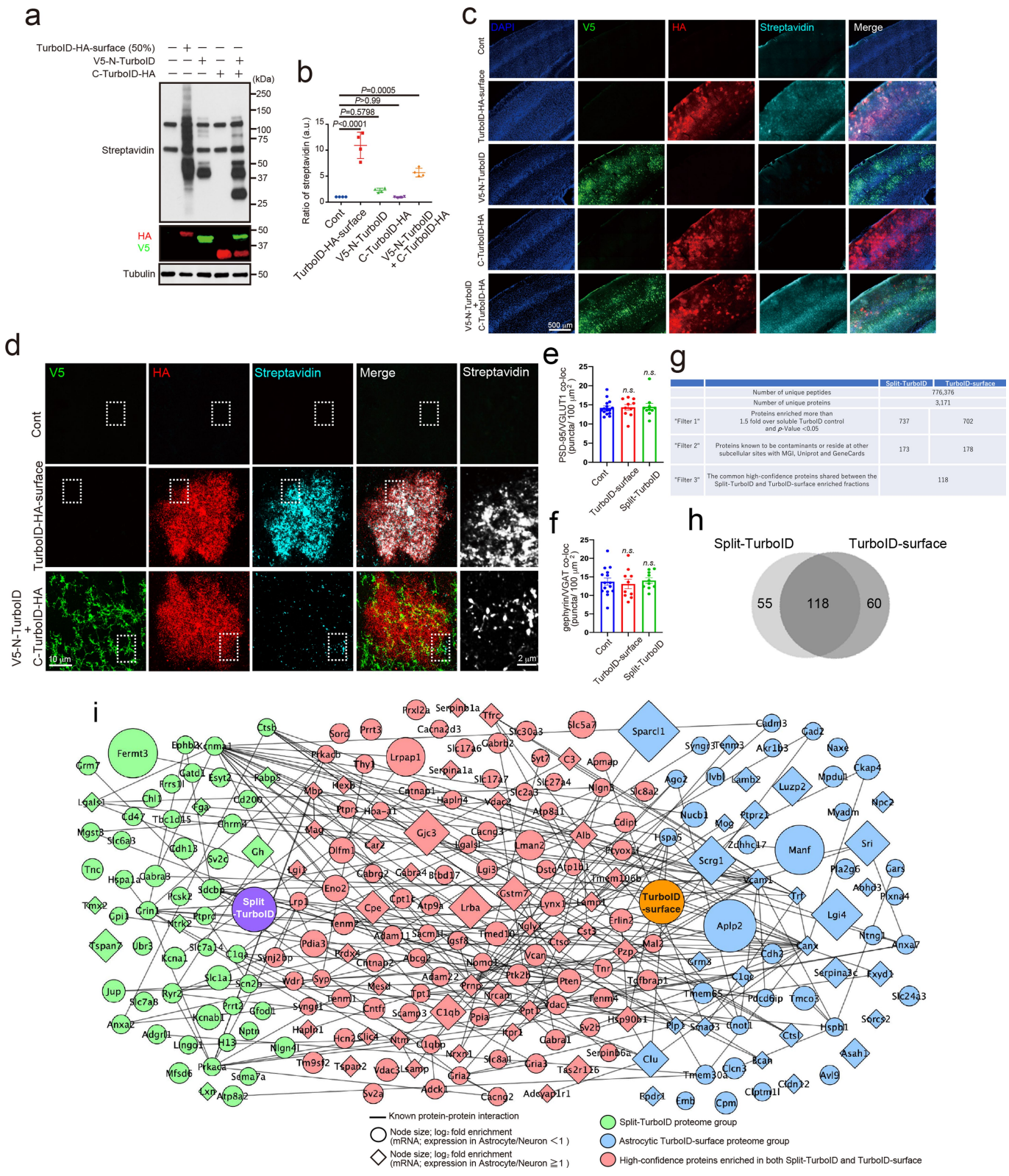

Extended Data Fig. 4 | See next page for caption.

Extended Data Fig. 4 | Mapping and identification of tripartite synaptic cleft proteins by Split-TurboID in vivo. a, Biotinylation activity of Split-TurboID in vivo. Lysates of mouse brain infected with cell-type-specific TurboID-surface-HA, V5-N-TurboID and/or C-TurboID-HA. Brain lysates were analysed by immunoblotting with anti-Streptavidin, anti-V5, anti-HA and anti-Tubulin antibodies. **b**, The graph indicates the ratio of botinylation activity in vivo ($n = 4$ brains per each condition). **c**, **d**, The biotinylation of Split-TurboID in mouse cortex. **e**, **f**, Quantification of average number of excitatory or inhibitory synaptic colocalized puncta in layer 2/3 of the visual cortex. $n = 15$ slices per each condition from 3 mice. **g**, Chart summarizing proteomic data set identified by mass spectrometry and filters used to identify top candidates. **h**, Venn diagram comparing proteome list of Split-TurboID and TurboID-surface. **i**, Scale-free network of Split-TurboID (green) and TurboID-surface (blue) identified proteins. High-confidence proteins enriched in both Split-TurboID and TurboID-surface fractions are shown in red. Neuronal enriched proteins (RNA-seq expression ratio <1) and astrocyte enriched proteins (RNA-seq expression ratio≧1.0) are represented as circle or diamond, respectively. At least $n = 4$ biological repeats. One-way ANOVA (Dunnett's multiple comparison, $P < 0.0001$, 0.001). Data are means ± s.e.m.

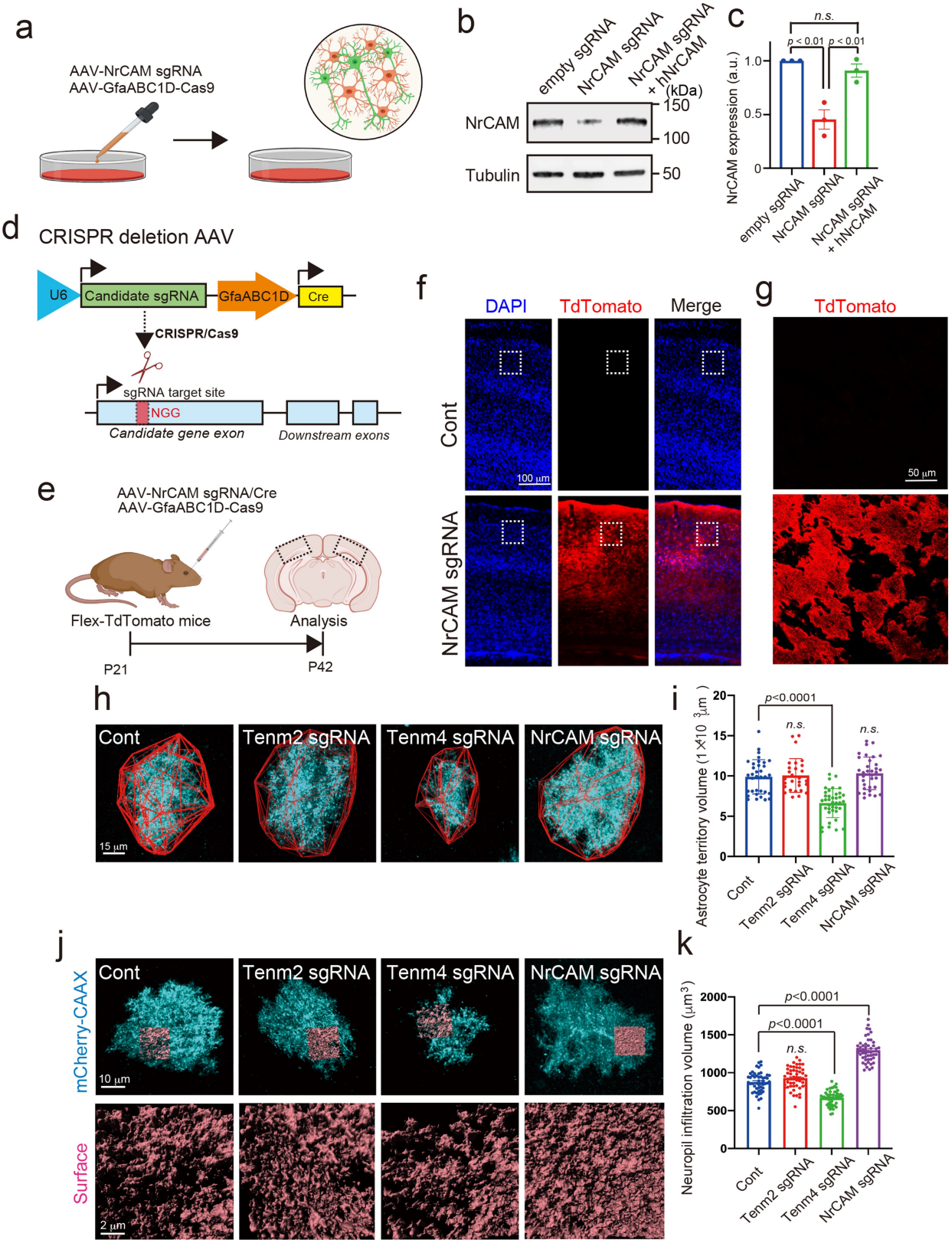

Extended Data Fig. 5 | See next page for caption.

Extended Data Fig. 5 | The validation of candidate proteins with CRISPR-based astrocytic candidate gene depletion strategy. a, Schematic of CRISPR-based deletion of astrocytic NrCAM in vitro. **b**, Immunoblots showing loss of NrCAM with sgRNA. AAV1/2-U6-empty sgRNA or AAV1/2-U6-NrCAM sgRNA was co-infected with AAV1/2- GfaABC1D-Cas9 to cultured neurons and astrocytes at DIV14. The cells were subjected to immunoblot analysis with an anti-NrCAM antibody. Tubulin was used as a loading control. **c**, The bar graph indicates the expression level of NrCAM from 3 independent experiments. **d**, Schematic of CRISPR-based deletion strategy of candidate gene. **e**, Experimental timeline of AAV-mediated CRISPR-based astrocytic gene deletion strategy in Flex-TdTomato mice. **f**, AAV PHP.eB-U6-NrCAM sgRNA was co-infected with AAV PHP.eB-GfaABC1D-Cas9 in Flex-TdTomato mice at P21. Coronal sections were prepared and immunostained with an anti-TdTomato antibody. **g**, A High-magnification image is shown. **h**, Images of Tenm2-, Tenm4- or NrCAM-deleted astrocytes (cyan) and their territories (red outlines) in visual cortexes of juvenile mice. **i**, Average territory volumes at P42 of Tenm2-, Tenm4- or NrCAM-deleted astrocytes. Between 20-25 cells per condition from 3 mice. **j**, Images of Tenm2-, Tenm4- or NrCAM-deleted astrocytes (cyan) and their NIV reconstructions (orange) in visual cortexes of juvenile mice. **k**, Average NIV at P42 of Tenm2-, Tenm4- or NrCAM-deleted astrocytes. 51 cells per each condition from 3 mice. $n = 3$ biological repeats. One-way ANOVA (Dunnett's multiple comparison, $P < 0.0001, 0.01$). Data are means ± s.e.m.

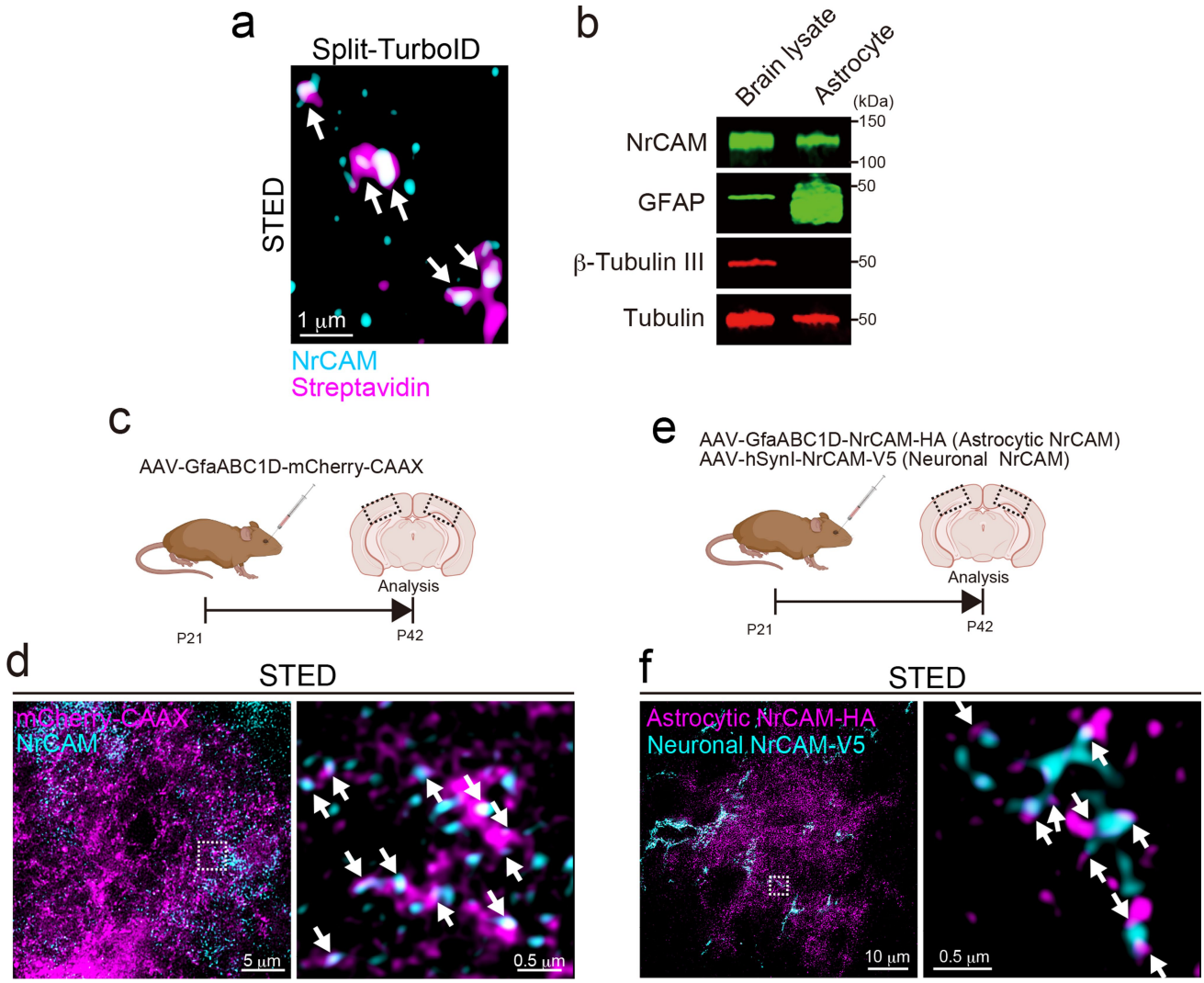

Extended Data Fig. 6 | NrCAM is a novel tripartite synaptic protein. a, A high magnification STED image showing that endogenous NrCAM was enriched at biotinylated proteins in vivo. **b**, Immunoblot analysis of endogenous NrCAM, astrocyte marker GFAP, neuronal marker b-Tubulin III or loading control α-Tubulin from mouse brain or purified astrocyte lysate. **c**, Schematic of the visualization of astrocytic membrane and endogenous NrCAM in vivo. **d**, STED images demonstrating the localization of endogenous NrCAM in vivo. Coronal sections were immunostained with anti-NrCAM antibody (cyan). High magnification image was shown (right panel). **e**, Schematic of the visualization of both astrocytic and neuronal NrCAM in vivo. **f**, STED images demonstrating that the colocalization of astrocytic NrCAM with neuronal NrCAM in vivo. Coronal sections were prepared and co-immunostained with an anti-V5 (cyan) and anti-HA (magenta) antibody. A high-magnification image is shown in the right. $n = 3$ biological repeats. Data represent means ± s.e.m.

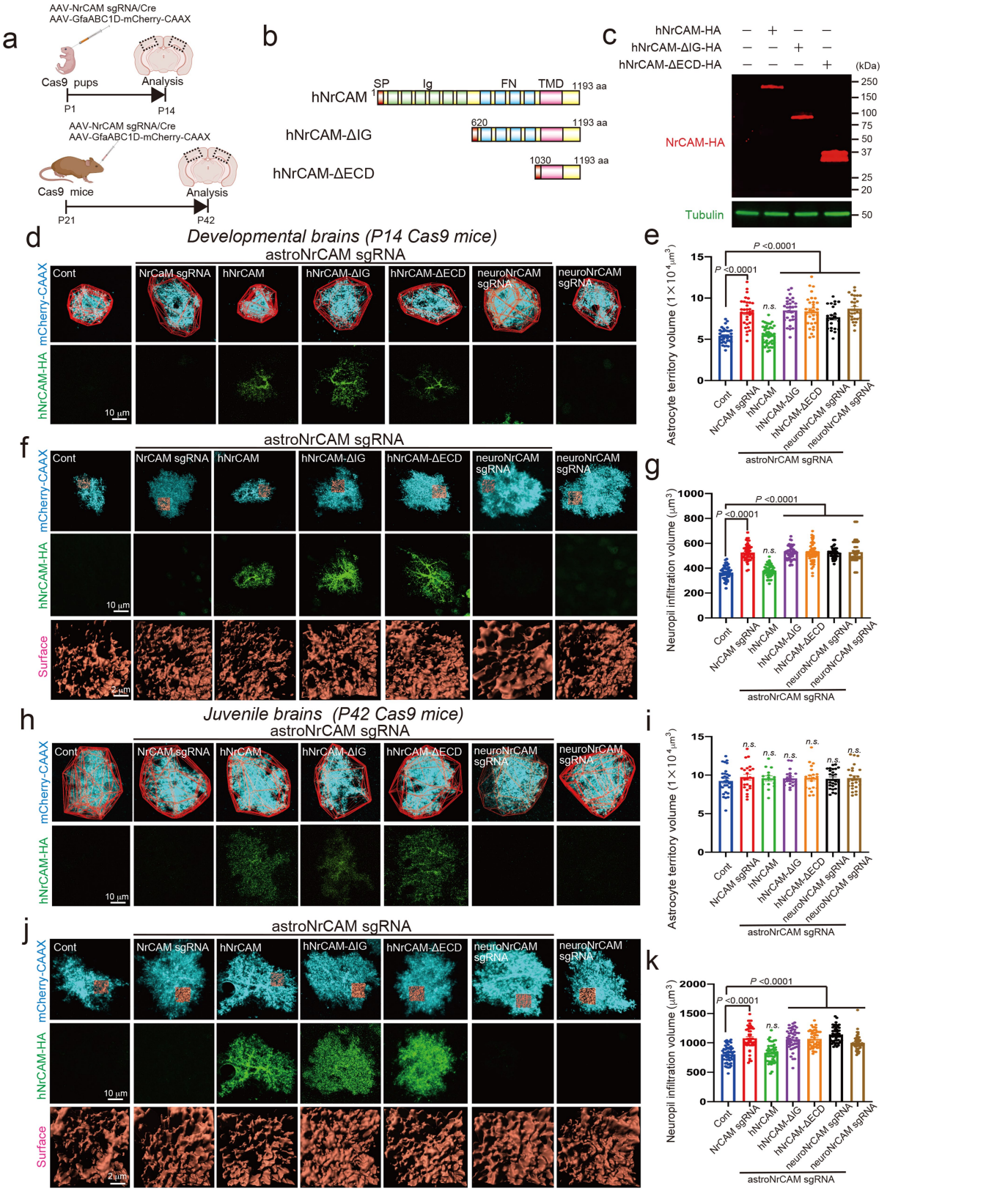

Extended Data Fig. 7 | The role of astrocytic NrCAM in astrocytic morphogenesis in vivo. a, Schematic of CRISPR-based NrCAM deletion in vivo. **b**, Schematic of hNrCAM domains and fragments. SP, signal peptide; IG, immunoglobulin; FN, fibronectin; TMD, transmembrane domain; ECD, extracellular domains. **c**, Immunoblots showing the expression of each NrCAM fragments in HEK293T cells. **d**, **f**, **h**, **j**, Images of astrocytes following deletion of astrocyte NrCAM alone (NrCAM sgRNA), with coexpression with indicated constructs of sgRNA-resistant human NrCAM, neuronal NrCAM deletion (neuroNrCAM sgRNA), or following neuronal NrCAM deletion alone. Images at indicated ages represent. **e**, **i**, Analysis of astrocyte territory, 15–29 cells per each condition from 3 mice; **g**, **k**, Analysis of neuropil infiltration volume. 50–51 cells per each condition from 3 mice. $n = 3$ biological repeats. One-way ANOVA (Dunnett's multiple comparison, $P < 0.0001$). Data represent means ± s.e.m.

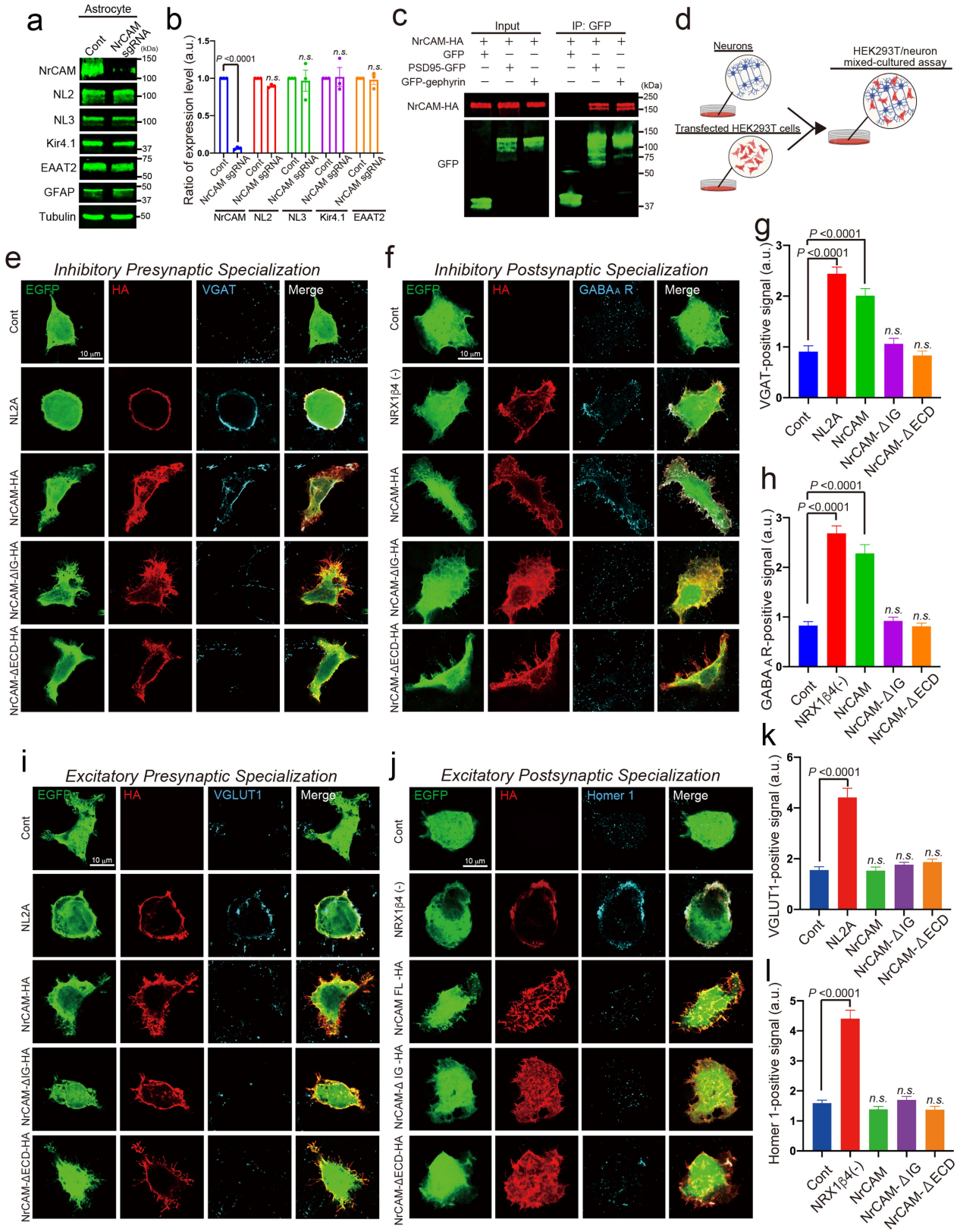

Extended Data Fig. 8 | See next page for caption.

Extended Data Fig. 8 | NrCAM controls inhibitory synaptic specializations through binding the gephyrin. a, Immunoblot analysis of endogenous NrCAM, astrocyte marker GFAP, Neuroligin 2, Neuroligin 3, Kir4.1 or EAAT2 (GLT1) from purified astrocyte lysate. **b**, The bar graph indicates the expression level. **c**, The interaction of NrCAM with PSD95 and gephyrin in HEK293T cells. Cell lysates coexpressing NrCAM-HA with GFP, PSD95-GFP or GFP-gephyrin were incubated with anti-GFP-bound beads. Immunoprecipitated (right) or total (left) NrCAM, GFP, PSD95-GFP or GFP-gephyrin were detected by immunoblotting with anti-HA and anti-GFP antibodies. **d**, Schematic of HEK293T/neuronal mixed-cultured assay in vitro. **e**–**h**, Images of in vitro inhibitory synapse formation assays. The graph shows average of the total integrated intensity of VGAT (Cont = 258, NL2 = 222, NrCAM = 242, NrCAM-ΔIG = 288, NrCAM-ΔECD = 303 cells) or GABAA receptor (Cont = 313, NRX1β4(-) = 310, NrCAM = 300, NrCAM-ΔIG = 278, NrCAM-ΔECD = 278 cells) clusters that contact transfected HEK293T cells. **i**–**l**, Images of in vitro excitatory synapse formation assay. The graph shows average of the total integrated intensity of VGLUT1 (Cont = 259, NL2 = 306, NrCAM = 286, NrCAM-ΔIG = 321, NrCAM-ΔECD = 196 cells) or HOMER1 (Cont = 471, NRX1β4(-) = 214, NrCAM = 247, NrCAM-ΔIG = 387, NrCAM-ΔECD = 251 cells) clusters that contact transfected HEK293T cells. $n = 3$ biological repeats. One-way ANOVA (Dunnett's multiple comparison, $P < 0.0001$). Data are means ± s.e.m.

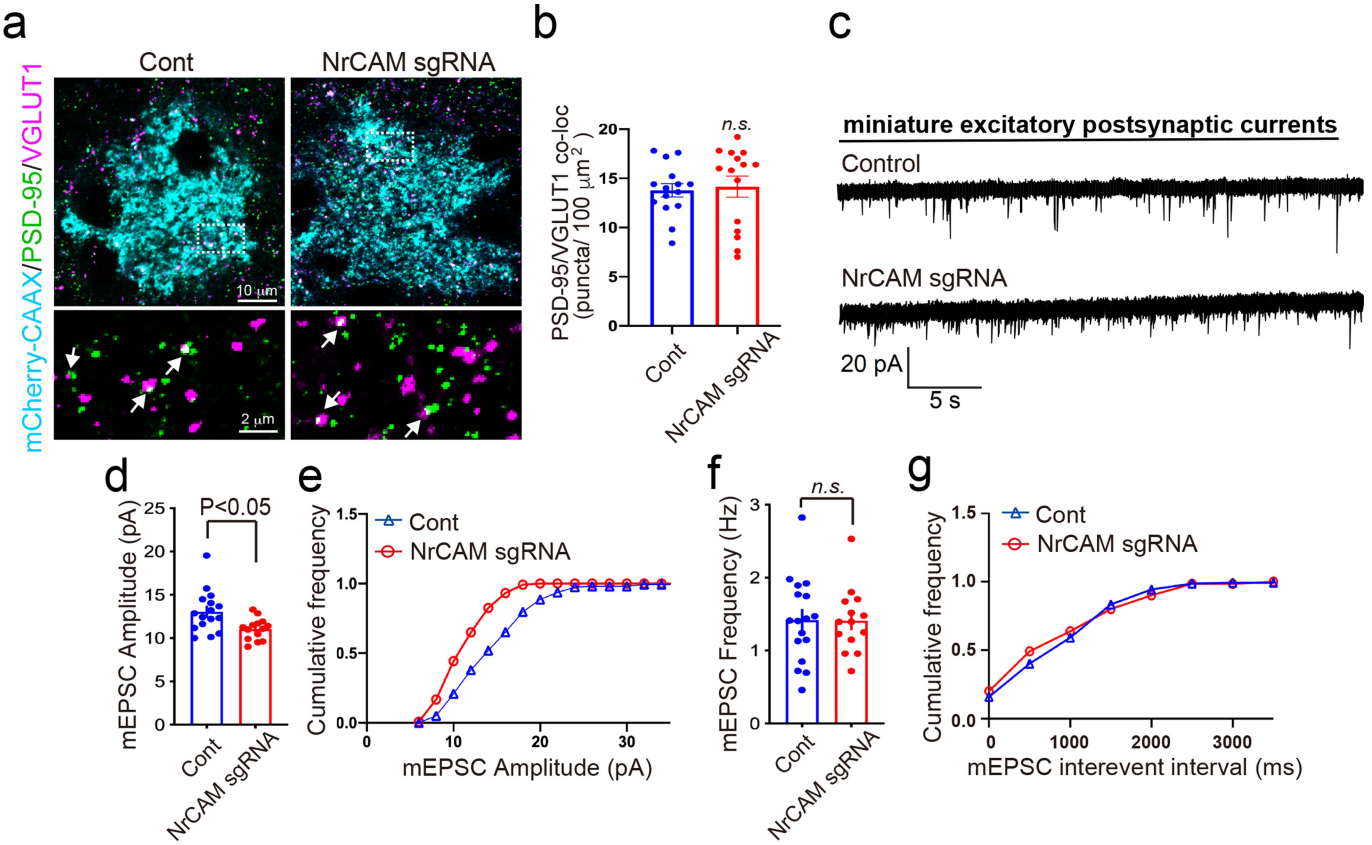

Extended Data Fig. 9 | The effect of NrCAM on excitatory synapse formation and function in vivo. a, Images of postsynapse PSD95 and presynapse VGLUT1 within NrCAM-deletion astrocytes in L1 of the visual cortex. High magnification images (bottom) correspond to boxes (above). **b**, Quantification of average number of excitatory synaptic colocalized puncta within astrocyte territories. $n = 15$ cells per each condition from 3 mice. **c**, mEPSC traces from L2/3 pyramidal neurons following astrocyte control empty sgRNA or NrCAM sgRNA expression. **d**–**g**, Quantification of mEPSC amplitude (**d**, **e**, Cont = 16, NrCAM sgRNA = 14 cells from 4 mice) and frequency (**f**, **g**, Cont = 14, NrCAM sgRNA = 17 cells from each of 4 mice). At least $n = 3$ biological repeats. Student's t-test (paired, $P < 0.05$). Data represent means ± s.e.m.

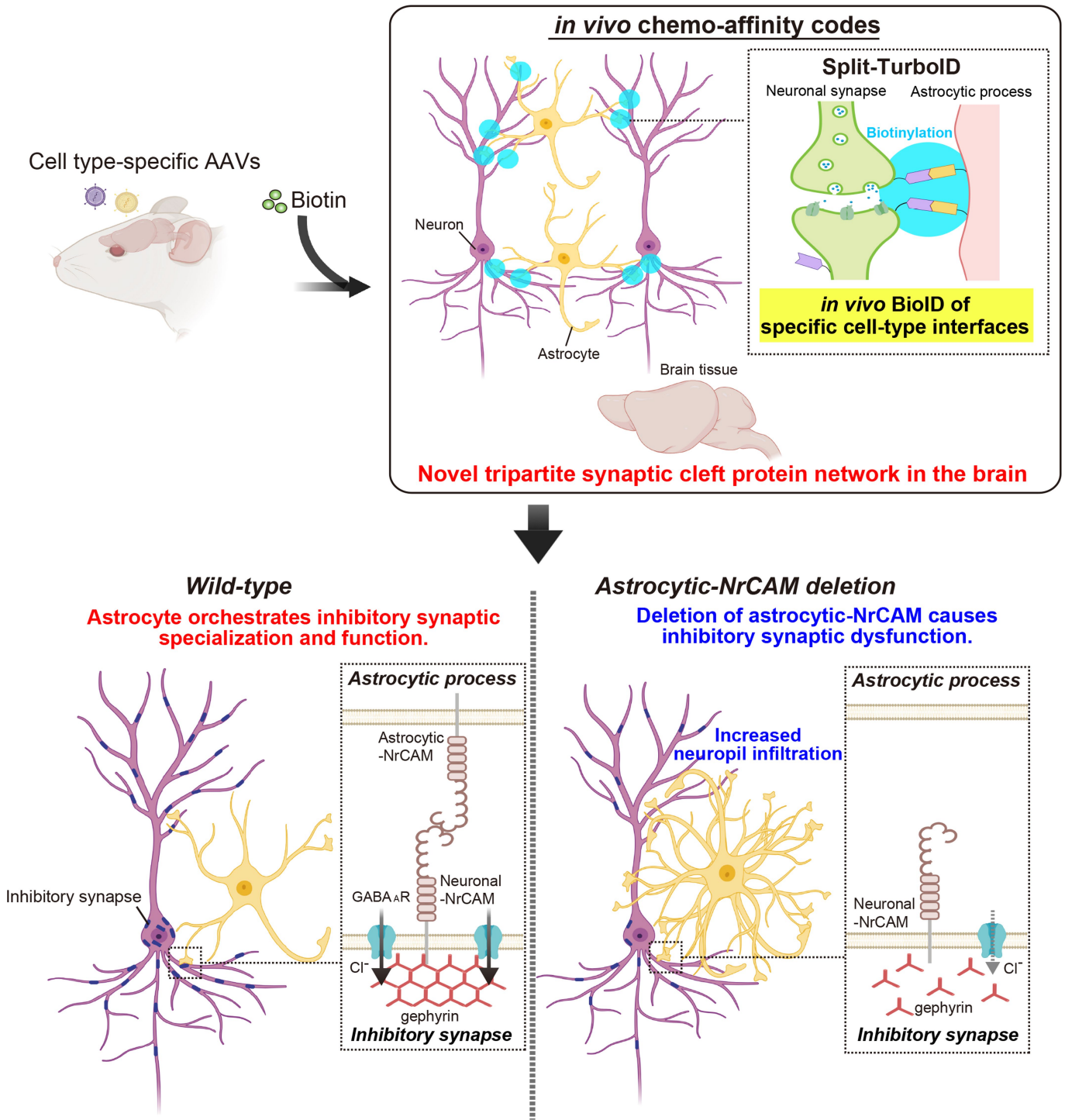

Extended Data Fig. 10 | In vivo chemogenetics method, Split-TurboID, reveals a novel astrocytic cell adhesion molecule, NrCAM, that controls inhibitory synaptic organization. Development of in vivo chemo-affinity codes, Split-TurboID, and a working model of astrocytic NrCAM influencing inhibitory synaptic function. Split-TurboID can map the molecular composition of such intercellular contacts, even within the highly complex structure of the tripartite synapse in vivo. Mapping this interface, we discovered a new molecular mechanism by which astrocytes influence inhibitory synapses within the tripartite synaptic cleft via NrCAM. NrCAM is expressed in cortical astrocytes where it interacts with neuronal NrCAM that is coupled to gephyrin at inhibitory postsynapses. Loss of astrocytic NrCAM dramatically alters inhibitory synaptic organization and function in vivo.

nature research

Corresponding author(s): Scott H. Soderling, Cagla Eroglu and Tetsuya Takano

Last updated by author(s): Jul 24, 2020

Reporting Summary

Nature Research wishes to improve the reproducibility of the work that we publish. This form provides structure for consistency and transparency in reporting. For further information on Nature Research policies, see our Editorial Policies and the Editorial Policy Checklist.

Statistics

For all statistical analyses, confirm that the following items are present in the figure legend, table legend, main text, or Methods section.

n/a	Confirmed
☐	☒ The exact sample size (*n*) for each experimental group/condition, given as a discrete number and unit of measurement
☐	☒ A statement on whether measurements were taken from distinct samples or whether the same sample was measured repeatedly
☐	☒ The statistical test(s) used AND whether they are one- or two-sided *Only common tests should be described solely by name; describe more complex techniques in the Methods section.*
☒	☐ A description of all covariates tested
☐	☒ A description of any assumptions or corrections, such as tests of normality and adjustment for multiple comparisons
☐	☒ A full description of the statistical parameters including central tendency (e.g. means) or other basic estimates (e.g. regression coefficient) AND variation (e.g. standard deviation) or associated estimates of uncertainty (e.g. confidence intervals)
☐	☒ For null hypothesis testing, the test statistic (e.g. *F*, *t*, *r*) with confidence intervals, effect sizes, degrees of freedom and *P* value noted *Give P values as exact values whenever suitable.*
☒	☐ For Bayesian analysis, information on the choice of priors and Markov chain Monte Carlo settings
☒	☐ For hierarchical and complex designs, identification of the appropriate level for tests and full reporting of outcomes
☒	☐ Estimates of effect sizes (e.g. Cohen's *d*, Pearson's *r*), indicating how they were calculated

Our web collection on statistics for biologists contains articles on many of the points above.

Software and code

Policy information about availability of computer code

Data collection	Zen Software (Zen black 2.3, Zen black 2.1 SP3 FP1), Leica Application Suite (LAS) software(v3.5.5), Odyssey Software(v4), Proteome Discoverer 2.2 (Thermo Scientific Inc.), GraphPad Prism (v8) and pClamp (v10) were used for data collection.
Data analysis	Imaris software (v8.2.1.), Leica Application Suite (LAS) software (v3.5.5), ImageJ (v10.2), and Mascot Distiller and Mascot Server (v 2.5, Matrix Sciences) were used for data analysis. Minora Feature Detection alogrithm is part of the Protein Discover Package version2.2.

For manuscripts utilizing custom algorithms or software that are central to the research but not yet described in published literature, software must be made available to editors and reviewers. We strongly encourage code deposition in a community repository (e.g. GitHub). See the Nature Research guidelines for submitting code & software for further information.

Data

Policy information about availability of data

All manuscripts must include a data availability statement. This statement should provide the following information, where applicable:

- Accession codes, unique identifiers, or web links for publicly available datasets
- A list of figures that have associated raw data
- A description of any restrictions on data availability

The data that support the findings of this study are available from the corresponding author upon reasonable request.

Field-specific reporting

Please select the one below that is the best fit for your research. If you are not sure, read the appropriate sections before making your selection.

☒ Life sciences ☐ Behavioural & social sciences ☐ Ecological, evolutionary & environmental sciences

For a reference copy of the document with all sections, see nature.com/documents/nr-reporting-summary-flat.pdf

Life sciences study design

All studies must disclose on these points even when the disclosure is negative.

Sample size	Sample sizes were determined based on previous experience (Stogsdill et al., Nature, 2017) for each experiment to yield high power to detect specific effects. No statistical methods were used to predetermine sample size.
Data exclusions	No data were excluded from the analyses.
Replication	All attempts at replication (3-5 times) were successful.
Randomization	Allocation was random.
Blinding	Images data collection and statistical analyses were analyzed blinded to the experimental conditions.

Reporting for specific materials, systems and methods

We require information from authors about some types of materials, experimental systems and methods used in many studies. Here, indicate whether each material, system or method listed is relevant to your study. If you are not sure if a list item applies to your research, read the appropriate section before selecting a response.

Materials & experimental systems

n/a	Involved in the study
☐	☒ Antibodies
☐	☒ Eukaryotic cell lines
☒	☐ Palaeontology and archaeology
☐	☒ Animals and other organisms
☒	☐ Human research participants
☒	☐ Clinical data
☒	☐ Dual use research of concern

Methods

n/a	Involved in the study
☒	☐ ChIP-seq
☒	☐ Flow cytometry
☒	☐ MRI-based neuroimaging

Antibodies

Antibodies used	The following antibodies were used: monoclonal anti-V5 (ThermoFisher, R960-25, IB 1:1000, IF 1:500, IHC 1:500), rat anti-HA (Sigma, 12158167001, IB 1:1000, IF 1:500, IHC 1:200), mouse anti-HA (Biolegend, MMS-101P, IB 1:1000), chicken anti-GFP (Abcam, ab13970, IB 1:1000, IF 1:1000, IHC 1:1000), rabbit anti-mCherry (Abcam, ab167453, IF 1:500, IHC 1:500), rabbit anti-PSD95 (Life Techonologies, 51-6900, IHC 1:200), mouse anti-PSD-95 (ThermoFisher, 7E3, IB 1:1000), guinea pig anti-VGLUT1 (Synaptic Systems, 135-304, IF 1:1000, IHC 1:1000), rabbit anti-gephyrin (Synaptic Systems, 147-002, IF 1:1000, IHC 1:500), mouse anti-gephyrin (Synaptic Systems, 147-011, IB 1:1000, IF 1:300), guinea pig anti-VGAT (Synaptic System, 131-004, IF 1:1000, IHC 1:500), rabbit anti-NL2 (Synaptic System, 129-202, IB 1:500), rabbit anti-NrCAM (Abcam, ab24344, IB 1:1000, IHC 1:200), rabbit anti-Homer1 (Synaptic Systems, 160002, IF 1:2000), rabbit anti-GABA-A receptor 2 (Synaptic Systems, 224-803, IF 1:1000), goat anti-Neuropilin-2 (R & D Systems, AF567, IB 1:500), rat anti-tdTomato (Kerafast, EST203, IHC 1:1000), rat anti-Tubulin (Santa Cruz, sc-53029, IB 1:1000), rabbit anti-Ezrin (Cell Signaling, #3142, IHC 1:200), rabbit anti-EAAT2 (GLT1) (Alamone, AGC-022, IB 1:1000), rabbit anti-Kir4.1 (Alamone, APC-035, IB 1:500), rabbit anti-NL3 (Novus, NBP1-90080, IB 1:500), Alexa Fluor 488 Goat anti-Mouse (ThermoFisher, A32723), Alexa Fluor 488 Goat anti-Rabbit (ThermoFisher, A-11034), Alexa Fluor 488 Goat anti-Guinea pig (ThermoFisher, A11073), Alexa Fluor 488 Goat anti-Chicken (ThermoFisher, A-11006), Oregon Green 488 Goat anti-Rabbit (ThermoFisher, O-11038), Alexa Fluor 555 Goat anti-Rabbit (ThermoFisher, A21428), Alexa Fluor 568 Goat anti-Rat (ThermoFisher, A-11077), Alexa Fluor 594 Streptavidin (ThermoFisher, S11227), Alexa Fluor 647 Donkey anti-rabbit (ThermoFisher, A31573), Alexa Fluor 647 Goat anti-Chicken (ThermoFisher, A-21449), Alexa Fluor 647 Donkey anti-Guinea pig (Jackson ImmunoResearch, 706-605-148), Alexa Fluor 647 Streptavidin (ThermoFisher, S21374), Atto647N anti-Mouse (Sigma, 50185), Atto647N anti-rabbit (Sigma, 40839), Donkey anti-Goat IRDye 800CW (LI-COR, 926-32214), Goat anti-rat IRDye 800CW (LI-COR, 925-32219), Goat anti-Mouse IRDye 680RD (LI-COR, 925-6818).
Validation	1 monoclonal anti-V5 ThermoFisher R960-25 ELISA, Immunocytochemistry, Immunofluorescence, Immunoprecipitation, Western Blot Vender (IB, IF) 2 rat anti-HA Sigma 12158167001 ELISA, Immunocytochemistry, Immunofluorescence, Immunoprecipitation, Western Blot "Hougbing Liu et al., 2014. J AM Heart Assoc 20; 3(3) (IB)

Fimiani et al., 2015. Nucleic Acids Res 18;43(16) (IB, IF)
Stogsdill et al., 2017. Nature "
3 mouse anti-HA Biolegend MMS-101P western blot (WB), immunocytochemistry (ICC), immunoprecipitation (IP), and flow cytometry (FC). "Kim JY, et al. 2003. J Neurosci. 23:5561. (IP, WB)
Helliwell SB, et al. 2001. J Cell Biol. 153:649. (WB)
Bennett BD, et al. 2000. J Biol Chem. 275:37712. (IF, IP, WB)
Royer Y, et al. 2005. J. Biol. Chem. 29:27251. (FC)"
4 chicken anti-GFP Abcam ab13970 IHC-P, WB, IHC - Wholemount, IHC-FrFl, ICC/IF, IHC-Fr, IHC-FoFr Vender (IB, IF, IHC)
5 rabbit anti-mCherry Abcam ab167453 WB, ICC/IF, IHC-P "Stogsdill et al., 2017. Nature 551, 192-197 (IF, IHC)
Vender (IB, IF)"
6 rabbit anti-PSD95 Life Techonologies 51-6900 human mouse, rat ELISA, ICC, IF, IP, WB "Vender (IB, IF, IHC)
Stogsdill et al., 2017. Nature 551, 192-197 (IF, IHC)"
7 mouse anti-PSD-95 ThermoFisher MA1-046 human, mouse, rat, xenopus Flow, ICC, IF, IHC, IP, WB Vender (IF, IB)
8 guinea pig anti-VGLUT1 Synaptic Systems 135-304 rat, mouse, human, cow WB, IP, ICC, IHC, EM, FACS Vender (IB, IF, IHC)
9 rabbit anti-gephyrin Synaptic Systems 147-008 human, rat, mouse, pig, goldfish, zebrafish WB, IP, ICC, IHC Vender (ICC, IHC)
10 mouse anti-gephyrin Synaptic Systems 147-011 human, rat, mouse, pig, goldfish, zebrafish, chicken WB, IP, ICC, IHC, EM
"Davenport EC, Szulc BR, Drew J, Taylor J, Morgan T, Higgs NF, López-Doménech G, Kittler JT
Cell reports (2019) 268: 2037-2051.e6. 147 011 (WB, ICC, IHC)
Vender (ICC, IHC)"
11 guinea pig anti-VGAT Synaptic System 131-004 rat, mouse, zebrafish, ape WB, IP, ICC, IHC, EM Vender (WB, ICC, IHC)
12 rabbit anti-NL2 Synaptic System 129-202 human, rat, mouse, monkey, ape, cow WB, IP, ICC, IHC Stogsdill et al., 2017. Nature 551, 192-197 (IB)
13 rabbit anti-NrCAM Abcam ab24344 mouse, rat, human IHC-Fr, IHC-P, ICC/IF, WB, IP, IHC-FoFr Demynanenko et al., J Neurosci 34:1127-87 (IB, IHC)
14 rabbit anti-Homer1 Synaptic Systems 160002 human, rat, mouse WB, IP, ICC, IHC Vender (WB, ICC, IHC)
15 rabbit anti-GABA-A receptor b2 Synaptic Systems 224-803 rat, mouse WB, IP, ICC, IHC Vender (WB, ICC, IHC)
16 goat anti-Neuropilin-2 R & D Systems AF567 human, rat, mouse WB, IP, ICC, IHC, FACS Demynanenko et al., J Neurosci 34:1127-87 (IB)
17 rat anti-tdTomato Kerafast EST203 WB, ELISA, IF, IHC, IP "Stogsdill et al., 2017. Nature (IHC)
Vender (IF)"
18 rat anti-Tubulin Santa Cruz sc-53029 mouse, human, rat WB, IP, ICC, IHC, EM, FACS Vender (IB, IF, IHC)
19 rabbit anti-Ezrin Cell Signaling #3142 human, mouse, rat, monkey, bovine WB Vender (WB)
20 rabbit anti-EAAT2 (GLT1) Alamone AGC-022 human, mouse, rat ICC, IF, IHC, LCI, WB Vender (IB, IF, IHC)
21 rabbit anti-Kir4.1 Alamone APC-035 human, mouse, rat ICC, IF, IHC, IP, WB Vender (IB)
22 rabbit anti-NL3 Novus NBP1-90080 human, mouse, rat WB, IHC "Stogsdill et al., 2017. Nature 551, 192-197 (IB)
Vender (IB)"

Eukaryotic cell lines

Policy information about cell lines

Cell line source(s)	HEK293T cell line was obtained from the Duke Cell Culture Facility.
Authentication	The cell line was validated by STR testing.
Mycoplasma contamination	The cell lines were tested for mycoplasma contamination and were negative.
Commonly misidentified lines (See ICLAC register)	No commonly misidentified cell lines were used in the study.

Animals and other organisms

Policy information about studies involving animals; ARRIVE guidelines recommended for reporting animal research

Laboratory animals	P1~P42, male and female CD1 (022, Charles River), Cas9 (028239,JAX) and Ai14 (007914,JAX) mice. All animals were housed at 72F +/-2 degrees at 30-70% humidity.
Wild animals	This study did not involve wild animals.
Field-collected samples	This study did not involve samples collected from the field.
Ethics oversight	The Duke University Institutional Animal Care and Use Committee provided ethical approval and guidance.

Note that full information on the approval of the study protocol must also be provided in the manuscript.